ACTA

C

TECHNICA

Jing Li

ADVANCED HIGH AND LOW FIELD ^{1}H AND ^{129}XE NMR METHODS FOR STUDYING POLYMERIZATION, CURING AND PORE STRUCTURES OF GEOPOLYMERS

UNIVERSITY OF OULU GRADUATE SCHOOL;
UNIVERSITY OF OULU,
FACULTY OF TECHNOLOGY
FACULTY OF SCIENCE

ACTA UNIVERSITATIS OULUENSIS
C Technica 836

JING LI

**ADVANCED HIGH AND LOW FIELD
^{1}H AND ^{129}XE NMR METHODS FOR
STUDYING POLYMERIZATION,
CURING AND PORE STRUCTURES
OF GEOPOLYMERS**

Academic dissertation to be presented with the assent of
the Doctoral Programme Committee of Technology and
Natural Sciences of the University of Oulu for public
defence in the OP auditorium (L10), Linnanmaa, on 2
September 2022, at 12 noon

UNIVERSITY OF OULU, OULU 2022

Abstract

Geopolymers are three-dimensional aluminosilicate frameworks, synthesized from the aluminosilicate sources activated by alkali solutions under mild conditions. They are widely regarded as sustainable construction materials.

The understanding of geopolymer pore structures is important for their development. The mechanical properties of geopolymers depend on their pore structures. Currently, the pore structures are often studied using destructive methods, which cannot be used in longitudinal studies. Thus, new methods are required to characterize the time-dependent properties of geopolymers.

In this thesis, the following advanced ^{1}H and ^{129}Xe nuclear magnetic resonance (NMR) methods were applied to study the polymerization, curing, and pore structure of geopolymers: ^{1}H relaxometry, ^{1}H cryoporometry, ^{129}Xe spectroscopy, and ^{129}Xe relaxometry. As a result, several interconnected mesopores with different pore sizes were found. Additionally, three factors were found to affect the geopolymerization and pore structures: water-to-solid ratio (*w/s*), silicon-to-aluminum ratio (*Si/Al*), and NH_4OH posttreatment. High *w/s* favors large pore sizes and enhanced pore connectivity. Low *Si/Al* = 1 contributes to the formation of the zeolite phase, resulting from the formation of a gel phase with low *Si/Al* during geopolymerization. The NH_4OH posttreatment did not change pore sizes, but it did increase the level of pore connectivity.

Keywords: ^{129}Xe NMR, cryoporometry, geopolymer, geopolymerization, NH_4OH treatment, NMR spectroscopy, pore structure, relaxometry, Si-to-Al ratio, single-sided NMR, water-to-solid ratio

Li, Jing, Kehittyneet korkean ja matalan kentän ^{1}H ja ^{129}Xe NMR-menetelmät geopolymeerien polymeroitumisen, kovettumisen ja huokosrakenteiden tutkimiseen.

Tiivistelmä

Geopolymeerit ovat kolmiulotteisia alumiinisilikaattirakenteita, jotka syntetisoidaan alumiinisilikaattilähteistä, jotka aktivoidaan alkaliliuoksella miedoissa olosuhteissa. Niitä pidetään laajalti ympäristöystävällisinä rakennusmateriaaleina.

Geopolymeerihuokosrakenteiden ymmärtäminen on tärkeää niiden sovellusten kannalta. Geopolymeerien mekaaniset ja absorptio ominaisuudet riippuvat niiden huokosrakenteista. Tällä hetkellä huokosrakenteita tutkitaan yleensä destruktiivisilla menetelmällä, jolloin pitkittäistutkimus ei ole mahdollista. Tämän vuoksi geopolymeerien ajasta riippuvien ominaisuuksien karakterisointiin tarvitaan uusia menetelmiä.

Tässä väitöskirjassa geopolymeerien polymeroitumisen, kovettumisen ja huokosrakenteen tutkimiseen sovellettiin edistyneitä ^{1}H- ja ^{129}Xe NMR-menetelmiä: ^{1}H-relaksometriaa, ^{1}H-kryoporometriaa, ^{129}Xe-spektroskopiaa ja ^{129}Xe-relaksometriaa. Tutkimuksessa löydettiin useita toisiinsa liittyneitä mesohuokosia, joiden huokoskoko oli erilainen. Tutkimuksessa huomattiin, että geopolymeerien polymeroitumiseen ja huokosrakenteeseen vaikuttaa kolme tekijää: vesi/kiintoainesuhde (*w/s*), pii/alumiini suhde (*Si/Al*) ja jälkikäsittely NH$_4$OH:lla. Suuri *w/s* suosii suuria huokoskokoja ja parantaa huokosten kytkeytyneisyyttä. Matala *Si/Al* = 1 edistää zeoliittifaasin muodostumista, mikä johtuu sellaisen geelifaasin muodostumisesta, jossa on alhainen *Si/Al* geopolymeroinnin aikana. NH$_4$OH-jälkikäsittely ei muuttanut huokoskokoa, mutta lisäsi huokosten kytkeytyneisyyttä.

Asiasanat: ^{129}Xe NMR, geopolymeeri, geopolymerointi, huokosrakenne, kryoporometria, matalan kentän NMR, NH$_4$OH-käsittely, NMR-spektroskopia, relaksometria, Si-Al-suhde, vesi-kiintoainesuhde

Dedicated to my parents

Acknowledgements

I want to express my most sincere gratitude to my parents. They supported every decision of mine. Every time I encounter difficulties, they are always there to encourage me to conquer them. This thesis is dedicated to them.

Oulu, 31st of May, 2022   Jing Li

List of abbreviations and symbols

2D	two-dimensional
3D	three-dimensional
AAM	alkali-activated materials
BJH	Barret–Joyner–Halenda
CPMG	Carr–Purcell–Meiboom–Gill
FID	free induction decay
IR	inversion recovery
MAS	magic angle spinning
MIP	mercury intrusion porosometry
MOFs	metal–organic frameworks
NMR	nuclear magnetic resonance
PSD	pore size distribution
RF	radio frequency
S/V	specific surface area-to-pore volume ratio
SEM	scanning electron microscopy
Si/Al	Si-to-Al ratio
SR	saturation recovery
SS	solid state
T_1/T_2	T_1-to-T_2 ratio
TEM	transmission electron microscopy
VT	variable temperature
w/s	water-to-solid ratio

List of original publications

This thesis is based on the following publications, which are referred throughout the text by their Roman numerals:

I   Li, J., Mailhiot, S., Sreenivasan, H., Kantola, A. M., Illikainen, M., Adesanya, E., Kriskova, L., Telkki, V.-V., & Kinnunen, P. (2021). Curing process and pore structure of metakaolin-based geopolymers: Liquid-state ^{1}H NMR investigation. *Cement and Concrete Research*, 143, 106394. https://doi.org/10.1016/j.cemconres.2021.106394

II Li, J., Mailhiot, S., Sreenivasan, H., Kantola, A. M., Telkki, V.-V., & Kinnunen, P. (2022). ^{129}Xe NMR analysis reveals efficient gas transport between inborn micro-, meso- and macropores in geopolymers. *Cement and Concrete Research*, 155, 106779. https://doi.org/10.1016/j.cemconres.2022.106779

III Li, J., Mailhiot, S., Kantola, A. M., Niu, H., Sreenivasan, H., Telkki, V.-V., & Kinnunen, P. (2022). Longitudinal single-sided NMR study: silica-to-alumina ratio changes the reaction mechanism of geopolymer [Manuscript submitted for publication].

IV Li, J., Mailhiot, S., Alzeer, M. I. M., Luukkonen, T., Niu, H., Kantola, A. M., Telkki, V.-V., & Kinnunen P. (2022). The effect of NH_4OH treatment to the pore structure of geopolymer detected by 129Xe and 1H NMR method [Manuscript in preparation].

In the original publications, the author of this thesis was involved in conceptualization, designing, conducting experiments, analyzing data, and writing the first draft of the manuscript with the guidance of supervisors SM, VVT, PK, and AMK. In Paper I, EA helped to perform the MIP, and HS helped to perform the SSNMR and N_2 physisorption experiments. In Paper II, SM contributed equally as the author, and HS helped to perform the SSNMR and N_2 physisorption experiments. In Papers III and IV, HN helped to perform N_2 physisorption experiments. In Paper IV, TL provided the recipe of the material.

Contents

1   Introduction

1.1   Background

Geopolymers are three-dimensional (3D) aluminosilicate frameworks, synthesized from aluminosilicate sources activated by alkali solution under mild conditions [1]. They have the chemical structure of -Si-O-Al-O-Si-. As their building units have a disordered arrangement, they are known as amorphous zeolites [2].

Geopolymers have been widely regarded as sustainable construction materials [3]. They have an advantage over the most widely used cementitious materials, such as zero-CO_2 emission and higher compressive strength [4]. Recently, geopolymers have been used in other applications, such as catalysts [5], adsorbents [6], and solid battery electrolytes [7], benefiting from their excellent pore structures and low synthesizing price. Furthermore, the understanding of their pore structures is important for their development. It has been shown that their mechanical properties are related to their pore structures when they are used as construction materials [8]. Additionally, the pore structure also affects their performance in other applications [9].

In the past, many experimental methods were used to obtain information about the geopolymer pore structures. Thus, N_2 physisorption [10] and mercury intrusion porosimetry (MIP) [11] are two conventional methods use for measuring the pore size, pore volume, porosity, and surface area of geopolymers; however, they lead to the specimen destruction. Microscopy techniques, including scanning electron microscopy (SEM) and transmission electron microscopy (TEM), are able to give pore size estimates from two-dimensional (2D) images [12]. Furthermore, tomography techniques based on X-rays [13] and electrons [14] have been used to provide images of the 3D framework of geopolymer in a nondestructive manner, but they are more suitable for detecting the micron-scale pores. The utilization of both nondestructive and effective methods for investigating the pore structures of geopolymers on a full scale is required.

[1]H nuclear magnetic resonance (NMR) relaxometry of absorbed water is a nondestructive method to detect pore sizes and connectivity in cementitious materials [15, 16]. Additionally, ^{1}H NMR cryoporometry is a nondestructive method to measure pore size distributions (PSDs) [17]. [129]Xe NMR spectra are another efficient way to detect the pore structures of porous materials, as the [129]Xe chemical shift is very sensitive to the surrounding chemical and physical

environments of xenon atoms [18]. As these NMR methods have worked well in detecting the pore structures of the materials similar to geopolymers, it is worth applying them to the investigation of the geopolymers' pore structures.

1.2 Aims of thesis

This thesis aims to provide a comprehensive understanding of the pore structures of geopolymers by applying advanced NMR methods. Furthermore, the pore size and connectivity of geopolymers were studied. Additionally, the effects of many factors, including the water-to-solid ratio (*w/s*), Si-to-Al ratio (*Si/Al*), and posttreatment by NH_4OH to the pore structures and geopolymerization during the curing process were revealed.

1.3 Outline of thesis

This thesis contains the following five chapters:

– Chapter 1, "Introduction," gives an overview of the research background and clarifies the needs of these studies. The scope of this thesis is also highlighted.
– Chapter 2, "Geopolymers," gives a detailed introduction to geopolymers. Additionally, the lacking information related to the pore structures of geopolymers is provided.
– Chapter 3, "Nuclear Magnetic Resonance," explains the basic theories of the NMR methods used in this thesis. It introduces how ^{1}H relaxometry, cryoporometry, and various ^{129}Xe NMR methods can be used for detecting pore structures.
– Chapter 4, "Pore Structures of Geopolymers Detected by ^{1}H and ^{129}Xe NMR," describes the main contents of the four research parts, including methods, results, discussion, and conclusion.

    – Paper I: The evolution of pore structures during curing was monitored using ^{1}H relaxation measurements. The pore sizes and connectivity were detected using ^{1}H relaxometry, cryoporometry, and two conventional methods, N_2 physisorption, and MIP. Additionally, the effects of a narrow *w/s* range on the curing process and pore structure were investigated.

- Paper II: Various ^{129}Xe NMR methods were applied to measure the pore sizes and connectivity. The effects of a wider *w/s* range on the pore size and connectivity were studied.
- Paper III: The mechanism of geopolymerization was studied on a single-sided NMR device. The effect of *Si/Al* on the mechanism of geopolymerization was investigated.
- Paper IV: The effect of NH_4OH posttreatment on the pore structure of geopolymer was studied by combining ^1H and ^{129}Xe NMR.

- Chapter 5, "Summary and Conclusion" highlights the main findings and meanings of this thesis.

2   Geopolymers

Geopolymers are aluminosilicate polymers formed as three-dimensional (3D) frameworks [1]. The name geopolymer was introduced by the French scientist Prof. Joseph Davidovits [19]. Geopolymers are synthesized from aluminosilicate sources with highly concentrated aqueous alkali hydroxide under mild conditions, normally not exceeding 100 °C [20]. Hence, they are also ascribed as a group of alkali-activated materials. The frameworks of geopolymers are mainly combined with -Si-O-Si-, -Si-O-Al-, and -Al-O-Al- bonds and are consistent with silicate and aluminate tetrahedra in the form of $[SiO_4]^-$ and $[AlO_4]^-$ [2]. The silicate and aluminate tetrahedra are arranged in a disordered way (Fig. 1), which has been confirmed by ^{29}Si and ^{27}Al solid-state (SS) magic angle spinning (MAS) NMR [21]. Their chemical formula is described as $M_n[-(SiO_2)_z - AlO_2-]_n \cdot mH_2O$, where M is an alkali metal ions, such as Na or K. The presence of Al_3^+ in a tetrahedral environment makes geopolymers negatively charged, but it is balanced by alkali metal cations from the activating solution.

Geopolymers are widely known as construction and porous materials. A better understanding of their pore structures can accelerate both their academic and commercial development. The applications, study of pore structure, and geopolymerization, as well as the factors affecting the pore structures of geopolymers, will be introduced in more detail in the following sections.
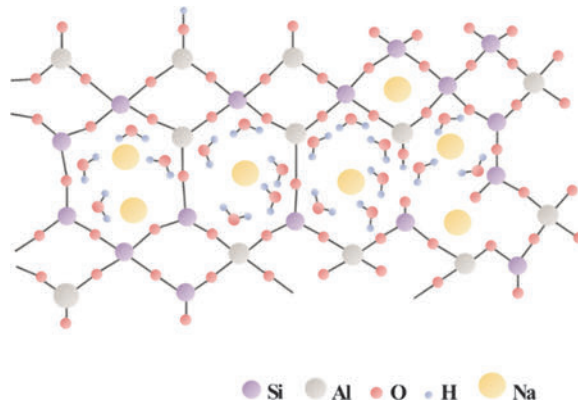
Fig. 1. Schematic structure of geopolymer synthesized from metakaolin and NaOH.

2.1 Applications

The two main applications of geopolymers will be introduced separately: One is working as construction materials and the other is usage as porous materials.

2.1.1 Construction materials

Geopolymers have been widely used as sustainable construction materials without CO_2 emissions [3]. They are expected to replace other conventional construction materials, i.e., cementitious materials. The cementitious material is one of the major emitters of CO_2, predicted to account for 25% of anthropogenic CO_2 emissions by 2025 [22]. When cementitious materials are made, the initial chemical reaction is the decomposition of $CaCO_3$ to CaO and CO_2, and the $CaCO_3$ comes from their raw material, limestone [23]. The raw materials of geopolymers are free of $CaCO_3$.

The use of geopolymers as construction materials has been also motivated by their excellent mechanical properties, such as compressive strength, flexural strength, and apparent density [4]. The compressive strength of geopolymers has been reported to reach up to 80 MPa [24].

Geopolymers also have many other desirable properties as construction materials. For example, they can retain high compressive strength after firing between 800 ℃ and 1000 ℃ [25]. This is due to their chemically bound water, which can migrate and evaporate to prevent damage to aluminosilicate frameworks. Geopolymers can also have long-term durability against aggressive environments, such as alkali attack, acid attack, chloride-induced corrosion, atmospheric carbonation, and freeze-thaw attack [26].

Low-calcium aluminosilicate geopolymers are a special class of alkali-activated materials (AAM), where the reaction mechanisms and reaction products are partially overlapping. The term geopolymer is used in scientific literature to refer to low-Ca aluminosilicates, while in other circles, it is often conflated with AAMs in general. While the low-Ca (<10 wt.% CaO) AAMs have been commercialized in high-value applications, such as in heat-resistant composites, the high-Ca AAMs have been commercialized in construction applications as a low-CO_2 alternative to Portland cement with superior durability [27]. The AAM concrete has been used over the past few decades in different parts of the world, the largest single application being the 70,000 tons pour at Brisbane airport in 2014 [28].

2.1.2 Porous materials

As mentioned before, geopolymers are often regarded as amorphous zeolites, as they include 3D frameworks consisting of silicate and aluminate tetrahedra, but the arrangements of these tetrahedra vary. Zeolites have an ordered arrangement, appearing in crystallite form, while geopolymers are arranged in a disordered way [29].

Furthermore, zeolites have been known globally as one of the most frequently used porous materials as adsorbents and heterogeneous catalysts [30]. They are also potential porous materials as they have similar frameworks as zeolites. Additionally, they process advantages over zeolites, such as low price and mild synthesis conditions.

There are two emerging utilizations taking advantage of their pore structure: One is the application as adsorbents, especially in the field of water treatment [6] and solid battery electrolyte [7]; another one is an application as catalysts, especially for the reduction of nitrogen oxides and oxidation of volatile organic compounds [5]. More applications of geopolymers as porous materials have been continuously explored.

2.2 Importance and characterization of pore structures

As geopolymers are regarded as both substitutes of conventional construction materials and excellent porous materials, it is important to understand their pore structures better. The most important porous properties of geopolymers are porosity, pore volume, pore size, pore connectivity, and specific surface area. The importance of understanding pore structures can be explained from two perspectives.

First, when geopolymers are used as construction materials, their mechanical properties are affected by the pore structure. Especially, the compressive strength is greatly affected by porosity [8]. The high porosity leads to low compressive strength. The permeability is highly dependent on the level of pore connectivity [31]. Additionally, the information about the growth of the pore structure during curing can also help to evaluate the feasibility of incorporating geopolymers into commercial production and knowing the setting duration during construction.

Second, the high porosity and high specific surface area-to-pore volume ratio (S/V) are two preconditions for advanced porous materials [32]. The pore size limits

the size of the guest molecules, and the pore connectivity determines whether the adsorbed guest molecule can reach targeted adsorbed/catalytic sites [9].

Many experimental methods have been used to study the pore structures of geopolymers. Thus, N_2 physisorption [10] and MIP [11] are two of the most popular conventional methods for detecting the pore structures of porous materials. N_2 gas and mercury are used as probes, respectively. They provide the PSD, pore volume, surface area, and pore size effectively. However, the powder specimen is required for N_2 physisorption. The wet geopolymer is in a gel state, and the dry geopolymer is in a block solid state, which means they need to be ground to powder when their pore structures are characterized by N_2 physisorption. Grinding may change the pore structures of geopolymers. Additionally, the MIP provides the throat size, not the real pore size [33].

The microscopic techniques, such as SEM and TEM (Figs. 2a and 2b), are characterization methods, which provide 2D images of the pores [12]. TEM provides higher resolution for material structure than SEM. The pore sizes can be estimated by both methods.

The tomography techniques (Fig. 2c) based on X-ray [13] and electrons [14] have been used to image the 3D frameworks of geopolymers in a nondestructive manner. They are not only able to provide the pore sizes, but the pore connectivity can be seen as well. They are good at detecting the pores in the scale of micrometers. The micropores and mesopores are out of their detection range.
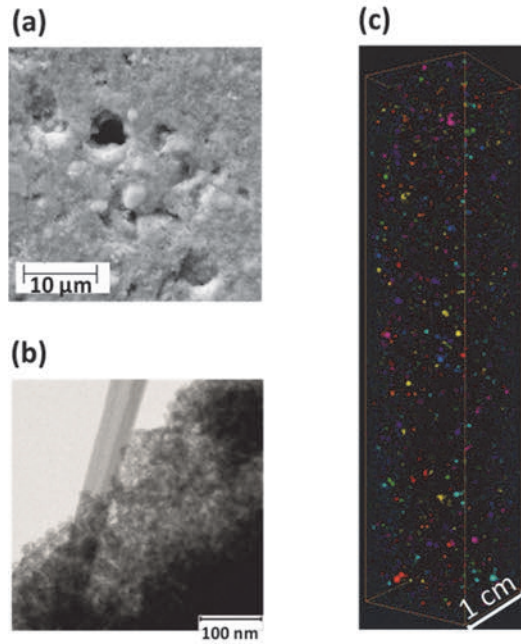
Fig. 2. Images of geopolymers acquired using (a) SEM, (b) TEM, and (c) X-ray tomography.

2.3   Geopolymerization

Geopolymers are formed by treating aluminosilicate precursors, such as metakaolin, fly ash, and slags, with high alkaline solution. The geopolymerization represents the growth process of the chemical and pore structures after reactants are mixed together [34]. The geopolymerization happens during the curing process, describing the setting process of geopolymers.

Many experimental methods have been used to study the mechanism of geopolymerization. ^{29}Si and ^{27}Al SSNMR spectroscopy [35], infrared spectroscopy, [36] and pair distribution function analysis [37] were applied to observe the evolution of chemical structures, and SEM with TEM were used to study the change of surface and inner porous structures during curing [38]. Differential scanning calorimetry was used to monitor the reaction heat flow [39]. The measurements of mechanical strength were also exploited to understand the geopolymerization [35]. By using these methods, many geopolymerization mechanisms were proposed.

25

In the 1950s, Glukhovsly proposed a general reaction mechanism consisting of three stages: destruction–coagulation, coagulation–condensation, and condensation–crystallization [40]. Later, researchers developed this mechanism into various versions according to the knowledge about the zeolite synthesis. All of them start from the dissolution of the precursors and end with the condensation of the whole structure, but the intermediate stages vary (Fig. 3). Next, the characteristics at different stages will be introduced.

Many studies have shown that the dissolution stage is present at the beginning of the geopolymerization. This is the stage where the precursors are dissolved into solutions under the effect of alkaline hydrolysis [34]. The precursors become Al and Si monomers, which are mainly in the species of $Al(OH)_4^-$, $OSi(OH)_3^-$, $(OH)_3$-Si-O-Al-$(OH)_3$, and so on [41]. Water is also consumed during this stage [34]. Following dissolution, some researchers also propose a stage for monomers to reach equilibrium, called speciation equilibrium [34].

The monomers then go through a series of intermediate dehydration reactions leading to a gel phase. Different studies proposed different numbers of dehydration stages, leading to different numbers of gel phases [40–48]. Two stages, gelation and reorganization, are proposed by some researchers [34, 35, 37] as shown in Fig. 3, and thus there are two gel phases. However, some other studies show only one phase formed from one gelation stage [44, 49, 50]. Gels result from a dehydration reaction. Some water molecules adsorbed during the dissolution stage are released during the intermediate dehydration reactions [34].

The formed gel continues to polymerize and condense to the solid polymer, which is also a dehydration reaction with water release [34]. Most of the proposed mechanisms finish here, but a little amount of the cured polymer was found to transfer to zeolite form following condensation [47].

Due to the complexity of geopolymerization, it is hard to say that it has been fully revealed. Additionally, as stated that various studies show different opinions to geopolymerization, more information should be acquired to boost them into commercial production.
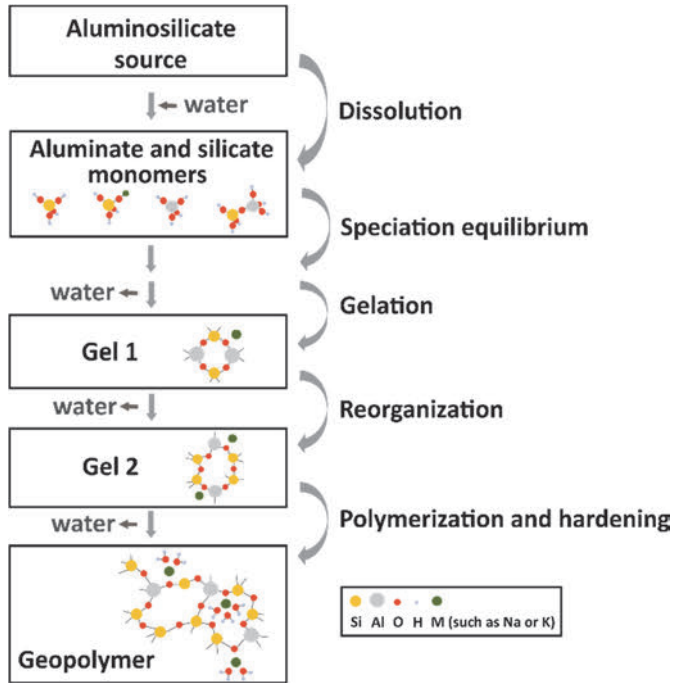
Fig. 3. Geopolymerization mechanism.

2.4 Factors affecting polymerization, structures, and properties of geopolymers

Many factors have been studied examine their effect on geopolymers. They can be classified into the following three types: 1. the ratios of the input of reactants, including w/s, Si/Al, and Si-to-Na ratio (Si/Na); 2. the type of aluminosilicate sources and alkali activators used for synthesis; and 3. the curing conditions, such as temperature and humidity [51]. Generally, these factors simultaneously affect geopolymerization, structure, and properties. When the duration and the detailed process of geopolymerization [52] are varying under the influence of these factors, the chemical and pore structures are prone to variations [53] because these two structures are grown from different geopolymerization processes. Porous properties, including the pore size, pore volume, porosity, and pore connectivity, are thus different. Pore structures have also been shown to affect the mechanical properties of the fresh and hardened geopolymers [54].

The effect of the ratio of the reactants will be introduced in more detail because interesting trends in how they affect the properties, pore structure, and geopolymerization have been revealed both in other studies and in this thesis. By tracing these trends, geopolymers can potentially be modified to a desired form. Thus, a deeper understanding of the influence of *w/s* and *Si/Al* are two objectives of this thesis.

The *w/s* is an important factor affecting the geopolymer formation, as water participates in the whole chemical reaction process during the curing process [53]. High initial *w/s* was found to accelerate the dissolution of raw materials and the hydrolysis of Si and Al species, because the amount of the chemical reaction medium, water, increases [56]. However, the gelation/polymerization and condensation stages were found to be slowed down with high *w/s* used, and thus the degree of polymerization is decreased [57]. Therefore, the *w/s* affects the pore structure significantly. With an increasing *w/s,* the porosity, pore size, and pore volume of geopolymer increase as well [58]. In the end, the compressive strength decreases as the *w/s* increases, and this is mainly because the porosity increases [59].

The *Si/Al* ratio is another important factor affecting the chemical structure of geopolymers. The structure of geopolymer with *Si/Al* of 1.7 has been proven to be stable and, simultaneously, the compressive strength is maximum [60]. In contrast, if the geopolymer is synthesized with an *Si/Al* >2.5, a dense structure is not formed, and thus the geopolymer has a low compressive strength [61]. Additionally, the *Si/Al* in the range 1.5–2 leads to a smaller pore size [62].

The *Si/Na* ratio has a great influence on the degree of polymerization of the dissolved species. The curing time of geopolymer increased when the *Si/Na* ratio increased from 0.4 to 0.8 because not enough alkali ions could be used to activate the Si species when the *Si/Na* is high [63]. The geopolymer formed from *Si/Na* over 1 has low strength due to poor reactivity of alkali solution [64], whereas the *Si/Na* of 0.75 leads to lesser porosity and high strength [65].

Although the effect of these ratios on the geopolymerization and pore structures of geopolymers has been studied many times, these studies are still limited to the traditional invasive characterization methods as stated in Sections 2.2 and 2.3. A development of nondestructive and information-rich characterization methods is needed to obtain a more exact and deeper understanding of the influence of these factors.

The effect of another factor on the pore structure of geopolymer, NH_4OH posttreatment, is also investigated in this thesis. Although there are many other

posttreatment methods used in zeolites modification, such as acid and strong alkali (NaOH) treatments, they tend to destroy pore structures of zeolites in a large scale. The NH_4OH treatment is a much milder process for modifying the pore structures of zeolites [66], and thus the effect of the NH_4OH treatment was selected. It was found that this treatment increases the size of micropores in the mesopore region and improves connectivity [67]. As geopolymers are amorphous zeolites, we aimed to figure out how the mild alkali treatment affects the geopolymers pore structure. This would provide a new way of modifying the geopolymers pore structure.

It is also reasonable that the different types of aluminosilicate sources and alkali activators used in synthesis lead to different structures and properties, providing different chemical composites [4]. The common aluminosilicate sources are metakaolin, fly ash, low-calcium slags, and mining wastes. Sodium hydroxide (NaOH) and potassium hydroxide (KOH) are the two most frequently used alkaline solutions [34]. Geopolymers studied in this thesis were prepared with metakaolin and NaOH. SiO_2 or sodium silicate solution were used to adjust the amount of SiO_2 contained in their structures.

3 Nuclear magnetic resonance

The NMR is a physical phenomenon at the atomic scale observed when nuclei are inserted into a strong magnetic field. To observe the signal, the nuclear spins are perturbed from equilibrium using radiofrequency radiation. As the spins return to equilibrium, a signal is observed. A more thorough treatment of NMR theory can be found in references [68–71].

The NMR is applied in the characterization of porous materials, such as silica gel [72, 73], cement-based materials [74, 75], zeolites [76–79], metal–organic frameworks (MOFs) [80, 81], carbon nanotubes [82, 83], and supramolecular materials [84]. The most common application of NMR is in the determination of chemical structures based on chemical shift information. Less common NMR techniques include relaxometry, cryoporometry, and [129]Xe NMR, which can be used to detect information about porous structures nondestructively. The following sections will describe the theories and applications of these NMR techniques in more detail.

3.1 Basics of NMR

Nuclei with nonzero spin have a magnetic moment $\boldsymbol{\mu}$ detected by NMR. The magnetic moment is written as

$$\boldsymbol{\mu} = \gamma \boldsymbol{I}, \tag{1}$$

where γ is the gyromagnetic ratio of the nucleus, and $\boldsymbol{I}$ is the spin angular momentum vector.

When the nucleus is placed in an external magnetic field along the z-axis, $\boldsymbol{B}_0$, the magnetic moment starts to precess around the $\boldsymbol{B}_0$ due to Zeeman interaction. This precession is called the *Larmor precession* [85]. The Larmor (angular) frequency is proportional to B_0 as

$$\omega_0 = \gamma B_0, \tag{2}$$

Furthermore, the orientations of $\boldsymbol{I}$ are quantized. The nucleus with spin quantum number I has $2I + 1$ orientations and each orientation can be represented by quantum number m. The quantum number m can have the following values of

$$m = I, I - 1, I - 2, \dots, -I. \tag{3}$$

For example, in the external magnetic field, the nucleus with $I = 1/2$ has two orientations, and thus they have two energy states, $m = 1/2$ and $m = -1/2$. The energy difference between the two states is (see also Fig. 4)

$$\Delta E_m = \frac{\gamma h B_0}{2\pi}.$$ (4)

where h is the Plank's constant.

For a system containing N nuclei, the total magnetization along the z-axis at thermal equilibrium ($M_{z,eq}$) is

$$M_{z,eq} = \frac{N\gamma^2 h^2 B_0 I(I+1)}{12\pi^2 kT}.$$ (5)

where T is the temperature, and k is the Boltzmann constant.

The magnetization vector is rotated away from the z-axis using a radio frequency (RF) pulse; its frequency is close to the Larmor frequency. After the perturbation, the magnetization of both processes around the z-axis takes place and approaches equilibrium due to a process called relaxation. The precession induces an oscillating voltage to detection coil, which is called the free induction decay (FID) signal. The time-domain signal is converted into the frequency-domain spectrum by the Fourier transformation

$$FT\{f(t)\} = F(\omega) = \int f(t)e^{-i\omega t}dt.$$ (6)
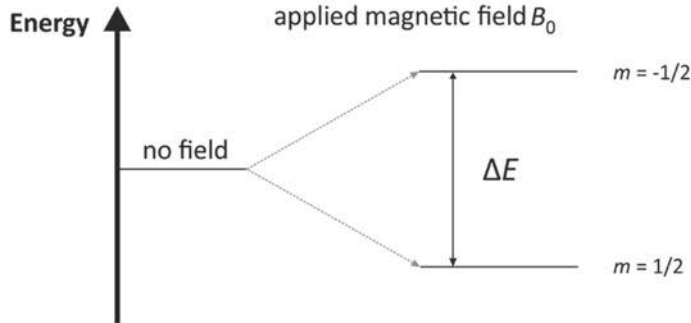
Fig. 4. Effect of Zeeman interaction on the energy levels of a nucleus with $I = 1/2$.

3.2 Chemical shift

In the NMR spectra, important information is conveyed by the chemical shift. When nuclei are inserted in an external magnetic field $\boldsymbol{B}_0$, this external field experienced by the nuclei is modified by the surrounding electrons. This shielding effect creates a local field of

$$\boldsymbol{B}_{\text{local}} = -\boldsymbol{\sigma} \cdot \boldsymbol{B}_0. \tag{7}$$

Here, $\boldsymbol{\sigma}$ is the shielding tensor. For a liquid sample, or when applying fast MAS on solid sample, the shielding tensor reduces into isotropic shielding constant, σ, and the resonance frequency of a nucleus, ω, is

$$\omega = \gamma_i B_0 (1 - \sigma), \tag{8}$$

where σ is the shielding constant. When nuclei are in different chemical environments, they have a slightly different ω. A dimensionless relative value chemical shift (δ) in parts per million (ppm) unit is introduced to reflect this as

$$\delta = \frac{\omega_{\text{sample}} - \omega_{\text{ref}}}{\omega_{\text{ref}}} \times 10^6, \tag{9}$$

Here, ω_{ref} is the frequency of a reference compound. For example, tetramethylsilane is often used as a reference compound for ^{1}H, ^{13}C, and ^{29}Si spectra. Chemical shift is used to distinguish different components in the system according to their different local chemical environments.

3.3 Relaxation

Relaxation times are other indicators to figure out the different components in the system. With the application of a RF field, nuclear magnetization is rotated from the external field direction toward the transverse direction. After this extra field is removed, the magnetization returns gradually to equilibrium. This recovery is described by the so-called relaxation times, and this physical recovery process is relaxation [86, 87]. This thesis studies two relaxation times: longitudinal relaxation time, called T_1 or spin–lattice relaxation time, and transverse relaxation time, called T_2 or spin–spin relaxation time.

3.3.1 Longitudinal relaxation

The T_1 relaxation describes the recovery of the longitudinal magnetization to thermal equilibrium ($M_{z,eq}$) according to

$$M_z(t) = M_{z,eq} - \left[M_{z,eq} - M_z(0)\right]e^{-\frac{t}{T_1}}. \qquad (10)$$

The T_1 values can be measured by inversion recovery (IR) [88] or saturation recovery (SR) [89] experiments. In the IR experiment (Fig. 5a), the magnetization is rotated to the $-z$-axis by a 180° pulse and $M_z(0) = -M_{z,eq}$. After time t_d, the recovered magnetization is read by a 90° pulse. For a single component system, the longitudinal magnetization obeys the equation (see Fig. 5c)

$$M_z(t) = M_{z,eq}\left(1 - 2e^{-\frac{t}{T_1}}\right). \qquad (11)$$

In the SR experiment (Fig. 5b), the magnetization can be rotated to the xy plane in many ways. The saturation section includes one or several 90° RF pulses and potentially also gradient pulses. Another 90° pulse is employed to read the recovered magnetization after time t_d (Fig. 5d). The equation becomes

$$M_z(t) = M_{z,eq}\left(1 - e^{-\frac{t}{T_1}}\right). \qquad (12)$$

The longitudinal relaxation happens due to the interaction of the spins with surrounding environment, and thus it is also called the "spin–lattice relaxation". In this thesis, the ^{1}H T_1 of water were measured by the SR pulse sequence as shown in Fig. 5b and ^{129}Xe T_1 of xenon were measured by IR experiments (Fig. 5a).
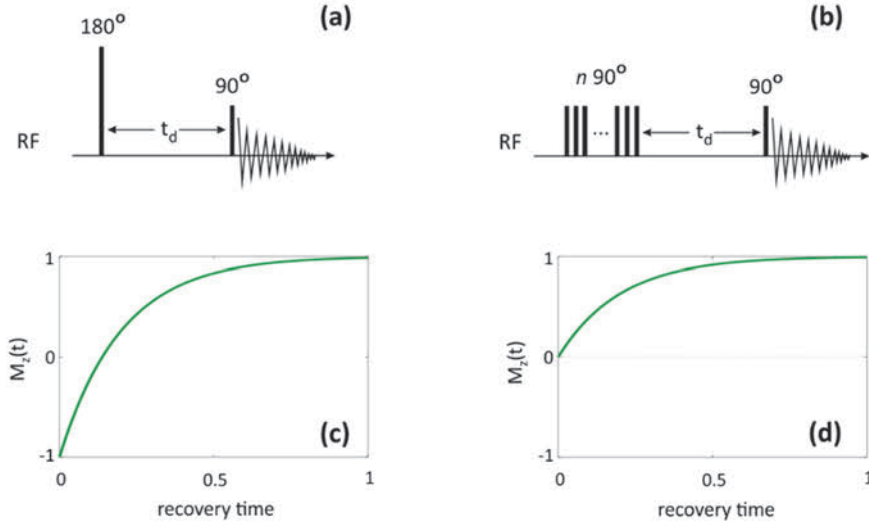
Fig. 5. (a) IR and (b) SR pulse sequences and the recovery of magnetization as a function of time in the (c) IR and (d) SR experiments, respectively.

3.3.2 Transverse relaxation

The T_2 relaxation describes the recovery of the transverse magnetization (M_{xy}) to thermal equilibrium state ($M_{xy,eq}$) and at the equilibrium, $M_{xy,eq} = 0$. In the rotating frame, transverse magnetization of a single component system decays to zero according to the equation

$$M_{xy}(t) = M_{xy}(0)e^{-\frac{t}{T_2}}. \tag{13}$$

The T_2 values are often measured by using the Carr–Purcell–Meiboom–Gill (CPMG) pulse sequence [90] (Fig. 6a). The CPMG pulse sequence consists of a 90° excitation pulse along the x-axis and n 180° refocusing pulses along the y-axis. The duration between 180° pulses is 2τ. The signal is observed as an exponential (Fig. 6b).

The essence of the transverse relaxation is the decoherence of the nuclear spins. In detail, the heterogeneous local fields result in varying precession frequencies, and there is loss of the coherence between the spins. T_2 is also called the "spin–spin relaxation."

(a)

1st   2nd   3rd   4th   5th   nth
180°$_y$ 180°$_y$ 180°$_y$ 180°$_y$ 180°$_y$ 180°$_y$

90°$_x$

RF

τ | 2τ | 2τ | 2τ | 2τ

(b)
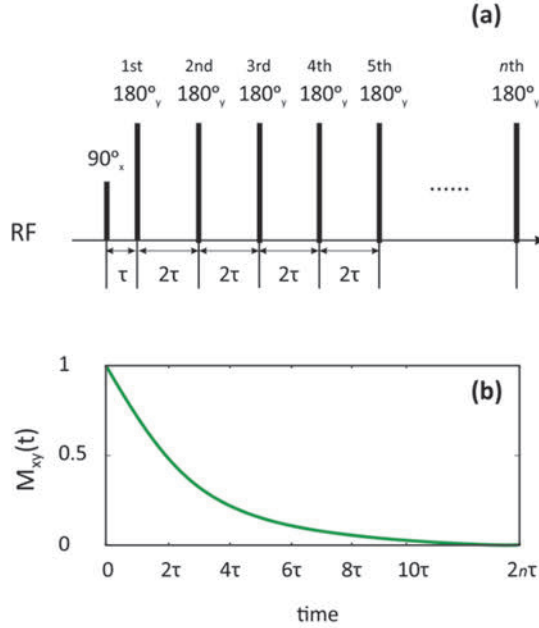
Fig. 6. (a) CPMG pulse sequence and (b) the evolution of magnetization during acquisition.

3.3.3 Relaxation time distribution

Here, T_2 and T_1 values obtained from single exponential fits are often shown as relaxation time distributions. The distributions were created by inserting the relaxation times and their standard deviations (SD) to the Gaussian function of

$$P = \frac{1}{SD\sqrt{2\pi}} \exp\left[-\frac{(x - T^2_{2 \text{ or } 1})}{2SD^2}\right]. \tag{14}$$

3.3.4 Pore size detection by relaxometry

Generally, T_1 and T_2 reflect the dynamics of the molecules. When T_1 and T_2 of liquid molecules in the pores are detected, the pore structures can be studied. When the liquid is confined in pores, a liquid layer with a thickness of ζ is in contact with the solid surface. The relaxation times of this liquid layer ($T_{1,2,\text{surf}}$) are decreased from the relaxation times of bulk liquid ($T_{1,2,\text{bulk}}$) [91]. Consequently, the average relaxation times of liquids in pores are shorter than of the liquid in free state [92].

36

The measured T_2 and T_1 ($T_{1,2,\text{measured}}$) of liquid molecules in pores are related to the S/V and surface relaxivity (ρ_{surf}), according to the equation

$$\frac{1}{T_{1,2,\text{measured}}} = \frac{1}{T_{1,2,\text{bulk}}} + \frac{S}{V}\rho_{\text{surf}}. \tag{15}$$

Here, $T_{1,2,\text{bulk}}$ is the T_1 or T_2 relaxation time of bulk liquid. The S/V reflects the pore size. For example, for the open cylindrical pore, $S/V = 2/r$, where r is the radius of the cylinder. ρ_{surf} is equal to $\zeta/T_{1,2,\text{surf}}$. Therefore, T_2 and T_1 reflect the pore size.

3.3.5 Surface affinity detection by relaxometry

Motion of a water molecule adsorbed on the surface of porous material is illustrated in Fig. 7. After the adsorption of the water molecule on the surface from the bulk water, it diffuses across the surface by moving between neighboring adsorption sites. This surface motion is represented by a diffusion correlation time, τ_{m}, averaged over all surface adsorbed molecules, and $1/\tau_{\text{m}}$ describes the time of transitions between adsorption sites. The molecule then desorbs back to the bulk water. This exchange between adsorbed and bulk water molecules is described by the surface residence time, τ_{s}.

At a low magnetic field, surface relaxation times are much shorter than bulk water relaxation times, i.e., $T_{1,2,\text{surf}} \ll T_{1,2,\text{bulk}}$. The $T_{1,\text{measured}}/T_{2,\text{measured}}$ is approximate to $T_{1,\text{surf}}/T_{2,\text{surf}}$, and it can be written as [93]

$$\frac{T_{1,\text{measured}}}{T_{2,\text{measured}}} \approx \frac{T_{1,\text{surf}}}{T_{2,\text{surf}}} = \frac{6\ln\left(\frac{\tau_s}{\tau_m}\right) + 5\ln\left[\frac{1+\omega_0^2\tau_m^2}{\left(\frac{\tau_m}{\tau_s}\right)^2 + \omega_0^2\tau_m^2}\right] + 2\ln\left[\frac{1+4\omega_0^2\tau_m^2}{\left(\frac{\tau_m}{\tau_s}\right)^2 + 4\omega_0^2\tau_m^2}\right]}{2\ln\left[\frac{1+\omega_0^2\tau_m^2}{\left(\frac{\tau_m}{\tau_s}\right)^2 + \omega_0^2\tau_m^2}\right] + 8\ln\left[\frac{1+4\omega_0^2\tau_m^2}{\left(\frac{\tau_m}{\tau_s}\right)^2 + 4\omega_0^2\tau_m^2}\right]}. \tag{16}$$

Therefore, T_1/T_2 is depends only on τ_{m} and τ_{s} for a given ω_0. As $\tau_{\text{s}}/\tau_{\text{m}}$ is a measure of surface affinity [94], T_1/T_2 reflects the strength of surface interaction between the water molecule and the pore surface [95].
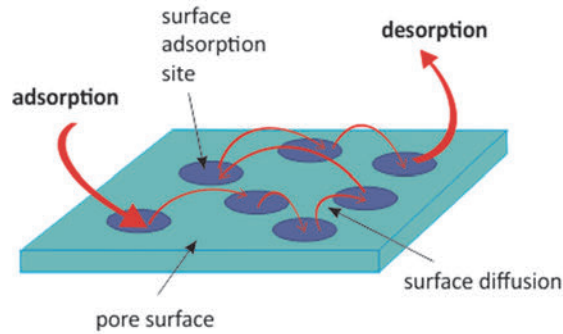
Fig. 7. Schematic of the motion of a water molecule adsorbed on a pore surface.

3.4 Two-dimensional relaxation experiments

With the development of the 2D Laplace inversion, the analysis of exponential data from 2D relaxation NMR experiments were made possible. These 2D relaxation NMR experiments have higher resolution for detecting different components or their changes than 1D experiments. 1D relaxation experiments measure single parameter, T_1 or T_2, while 2D relaxation experiments measure two parameters simultaneously. Thus, they allow for the measurement of correlation between the parameters. The most common 2D relaxation experiments are T_1–T_2 [96, 97] and T_2–T_2 [98] experiments.

The pulse sequence of a T_1–T_2 correlation experiment is a combination of IR or SR with CPMG experiments, and it is shown in Fig. 4. A 180° inversion pulse is used for IR (Fig. 8a), and n 90° pulses are used for SR (Fig. 8b); t_d is the delay for T_1 recovery, and the delay for T_2 decay is n times 2τ. The acquired signal is transformed by 2D Laplace inversion to 2D T_1–T_2 correlation spectra (Fig. 8c). The peak of free water is always aligning on the line of $T_1 = T_2$. The detected water phases confined in pores, such as A and B, align on the line of $T_1 = nT_2$. In this thesis, the pulse sequence shown in Fig. 8b was used to get all the T_1–T_2 maps.
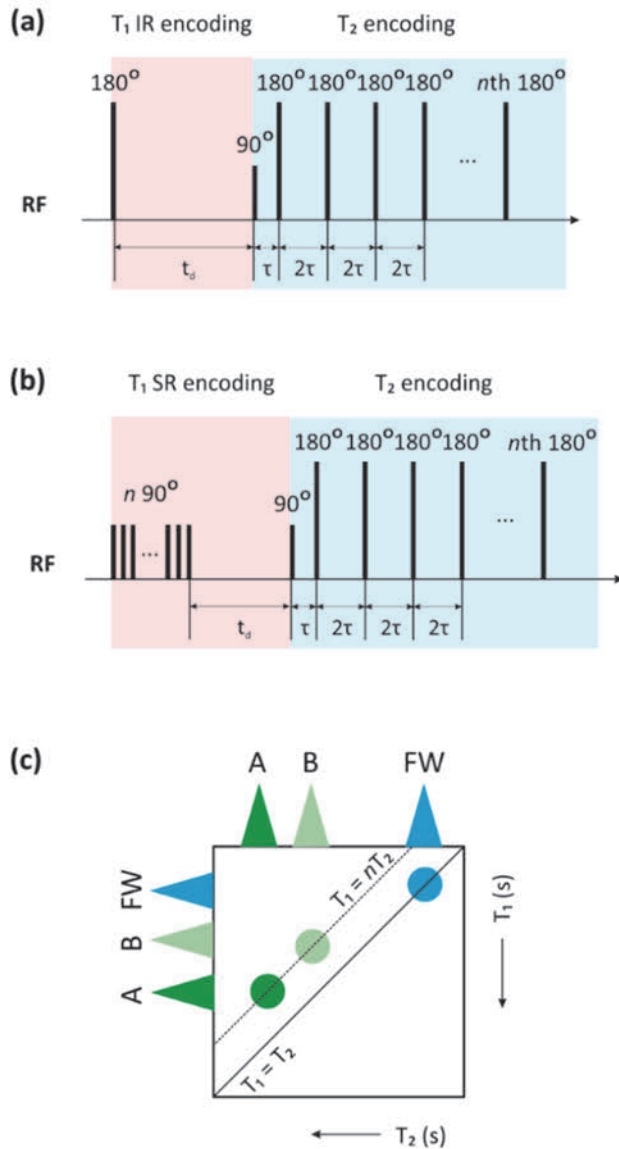
Fig. 8. (a) T_1IR–T_2 **pulse sequence, (b)** T_1SR–T_2 **pulse sequence, and (c) the schematic of a** T_1–T_2 **correlation map.**

The pulse sequence of T_2–T_2 exchange experiment is shown in Fig. 9a. It includes two CPMG loops separated by a delay τ_m. Before τ_m, signal decays due to $T_2^{(1)}$, and

after τ_m, if $T_2^{(1)} = T_2^{(2)}$, diagonal signals are observed (Fig. 9b). However, if there are two pools A and B in the system, and there is exchange between the pools during the τ_m, off-diagonal signals appear. For a porous system, the exchange peaks can reflect pore connectivity.
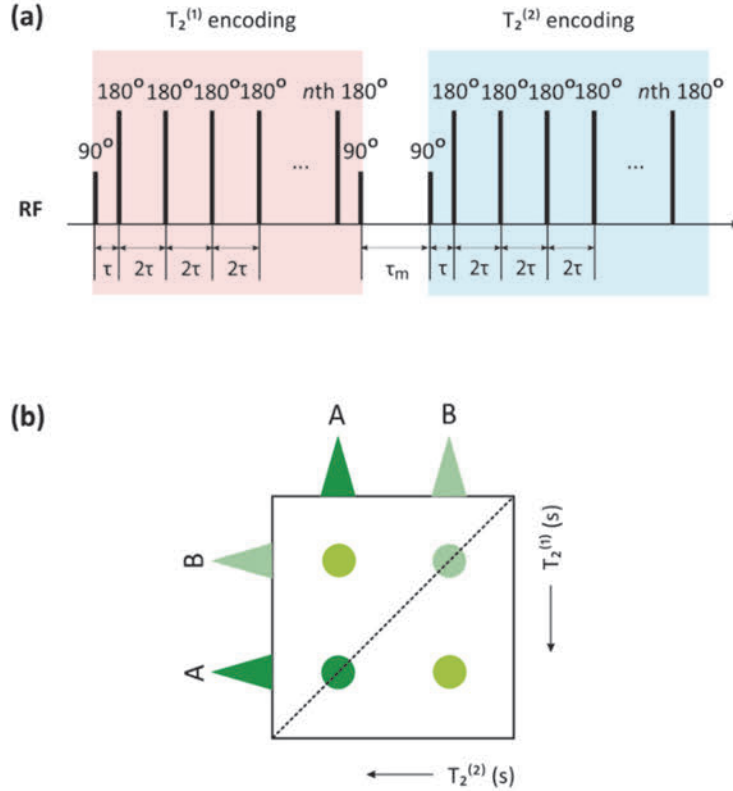
Fig. 9. (a) T_2–T_2 pulse sequence and (b) the schematic of a T_2–T_2 exchange map.

The signal S observed in 2D relaxation experiments as a function of encoding times t_{D1} and t_{D2} in the first and second dimensions can be written as

$$S(t_{D1}, t_{D2}) = \sum \exp\left(-\frac{t_{D1}}{T_{D1}}\right) \exp\left(-\frac{t_{D2}}{T_{D2}}\right) P(T_{D1}, T_{D2})$$
$$+ N(t_{D1}, t_{D2}), \tag{17}$$

in which T_{D1} and T_{D2} represent the relaxation times detected in the first and second dimensions, $P(T_{D1}, T_{D2})$ is the distribution of relaxation times and $N(t_{D1}, t_{D2})$ represents the signal noise.

40

In this thesis, all the 2D relaxation signals were converted into 2D distributions of relaxation times, also called 2D relaxation maps by a 2D Laplace inversion [99, 100]. In general, the Laplace inversion is an ill-posed problem and very sensitive to experimental noise. The inversion was made more stable and physically justified by a nonnegativity constraint, which allows only positive intensities in the relaxation map. Furthermore, unreasonable oscillation of the relaxation time distributions was reduced by using a regulator smoothing the distributions. The algorithm was accelerated by a singular value decomposition.

3.5 NMR cryoporometry

When a liquid is confined to a small pore, the melting temperature point is lowered according to the Gibbs–Thomson equation of [101, 102]

$$\Delta T_{\text{melting}} = T_{\text{melting}} - T_{\text{melting}}(a) = \frac{4\sigma_{\text{cl}} T_{\text{melting}}}{a \Delta H_f \rho_c}. \tag{18}$$

Here, $\Delta T_{\text{melting}}$ is the melting point depression, T_{melting} is the bulk melting temperature, $T_{\text{melting}}(a)$ is the melting temperature of the liquid in cylindrical pores with size of a, σ_{cl} is the frozen phase–liquid phase interfacial energy, ΔH_f is the bulk enthalpy of fusion, and ρ_c is the density of the frozen liquid. This equation can be rewritten as

$$\Delta T_{\text{melting}} = \frac{k}{a}, \tag{19}$$

where k is a constant dependent on the liquid. Hence, this physical phenomenon can be used to detect the pore size.

NMR cryoporometry is a thermoporometry method that detects the amount of liquid water at a range of temperatures. From this, the melting point distribution and thus PSD can be determined [103]. In a spin echo or CPMG experiment, the signal intensity S is proportional to the hydrogen content ρ_H as

$$S \sim \rho_H e^{-\frac{t}{T_2}}. \tag{20}$$

Here, t is the observation time. As the T_2 relaxation of ice is <10 μs [104], by using $t > 50$ μs, signal from the solid is eliminated, and thus S represents the volume of liquid water.

The PSD $\partial V/\partial a$ can be derived from the equation [105]

$$\frac{\partial V}{\partial a}(a) = \frac{\partial V}{\partial \Delta T_{\text{melting}}} \frac{\partial \Delta T_{\text{melting}}}{\partial a} = -\frac{k}{a^2} \frac{\partial V}{\partial \Delta T_{\text{melting}}} \sim -\frac{k}{a^2} \frac{\partial S}{\partial \Delta T_{\text{melting}}}, \tag{21}$$

where V is the volume of pores.

It has also been proposed that the signal intensity can be approximated by the function [106]

$$S(X) = \sum_{i=1}^{n} S_{0i} \left[1 - \text{erf}\left\{\frac{X - X_{ci}}{\sqrt{2}\sigma_i}\right\}\right]/2, \qquad (22)$$

where $X = 1000/T$, n is the number of phase transitions; S_{0i}, X_{ci}, and σ_i; are the intensity, $1000/T_{ci}$ and the width of the temperature distribution curve of phase i, respectively.

By differentiating Eq. 21 with respect to X, the melting point distribution curve dS/dX, which is a sum of Gaussian functions, is given by

$$\frac{dS}{dX} = -\sum_{i=1}^{n} \frac{S_{0i}}{\sqrt{2\pi}\sigma_i} \exp\left[-\left\{\frac{X - X_{ci}}{\sqrt{2}\sigma_i}\right\}^2\right]. \qquad (23)$$

The pore size distribution dS/da, obtained from Eqs. 18, 19, and 21, is

$$\frac{dS}{da} = \frac{10^3 k}{\sqrt{2\pi}(aT_{\text{melting}} - k)^2} \sum_{i=1}^{n} \frac{S_{0i}}{\sigma_i} \times \left[-\left\{\frac{10^3 a - X_{ci}(aT_{\text{melting}} - k)}{\sqrt{2}\sigma_i(aT_{\text{melting}} - k)}\right\}^2\right]. \qquad (24)$$

3.6 ^{129}Xe NMR

Xe has been often used as a probe gas in NMR experiments, because ^{129}Xe chemical shift is sensitive to the surrounding chemical and physical environment. Xe atom has a large electronic cloud and any distortion in the electronic cloud affects the chemical shift. When Xe gas is used in a porous system, ^{129}Xe chemical shift can be regarded as a sum of three major contributions [107]:

$$\delta = \delta_0 + \delta_{\text{Xe-solid}} + \delta_{\text{Xe-Xe}}. \qquad (25)$$

Here, δ_0 is the chemical shift at zero pressure, $\delta_{\text{Xe-solid}}$ is the chemical shift caused by Xe interacting with solid structure, and $\delta_{\text{Xe-Xe}}$ is the term representing the interactions between Xe atoms. In porous materials, the $\delta_{\text{Xe-solid}}$ term is dependent on the interaction of ^{129}Xe with the pore wall and is therefore dependent on the porous structure, such as S/V, a, and surface morphology. The $\delta_{\text{Xe-Xe}}$ term becomes larger as the Xe concentration grows. At the low gas pressure, it can be neglected.

3.6.1 Variable temperature measurements

^{129}Xe NMR spectra collected at variable temperature (VT) is a way to measure pore sizes and heats of adsorption. The ^{129}Xe chemical shift is proportional to S/V [108] as

$$\delta = \frac{\delta_a}{1+\frac{V}{SKRT}\frac{1}{}}.$$

(26)

Here, δ_a is the chemical shift of Xe adsorbed on the surface of pores, K is the Henry's constant, and R is the gas constant. K depends on the heat of adsorption Q:

$$K = \frac{K_0 \exp\left(\frac{Q}{RT}\right)}{T^{\frac{1}{2}}},$$

(27)

where K_0 is a preexponential factor.

3.6.2 2D EXSY

The 2D EXSY NMR provides information in exchange between different sites. The EXSY NMR includes two frequency axes (Fig. 10). The basic scheme of 2D NMR experiments includes four periods: preparation, evolution, mixing, and detection [68]. In the EXSY experiment [109] (Fig. 10), during the preparation period, there is a 90° pulse. After the evolution period t_1, two 90° pulses with the interval t_m form the mixing period, and then during t_2, there is the detection period.

In the EXSY spectra, there are diagonal and off-diagonal peaks. The diagonal peaks represent spins that did not exchange during the mixing period. The off-diagonal peaks represent spins that exchanged during the mixing period. Commonly, a set of spectra are acquired with variable t_m to see the appearance and the change of peaks, and to find the exchange time. In that sense, EXSY is a 3D experiment.

The EXSY experiment can detect both chemical and physical exchange processes. The exchange time scale needs to be longer than the NMR timescale, but shorter than T_1, so that the exchange can be resolved in the EXSY spectra. The NMR timescale is $1/(2\pi\Delta v)$, where Δv is the difference of the resonance frequencies of the nuclei [110].

By studying the exchange between Xe gas adsorbed in different pores, the pore connectivity can be understood.
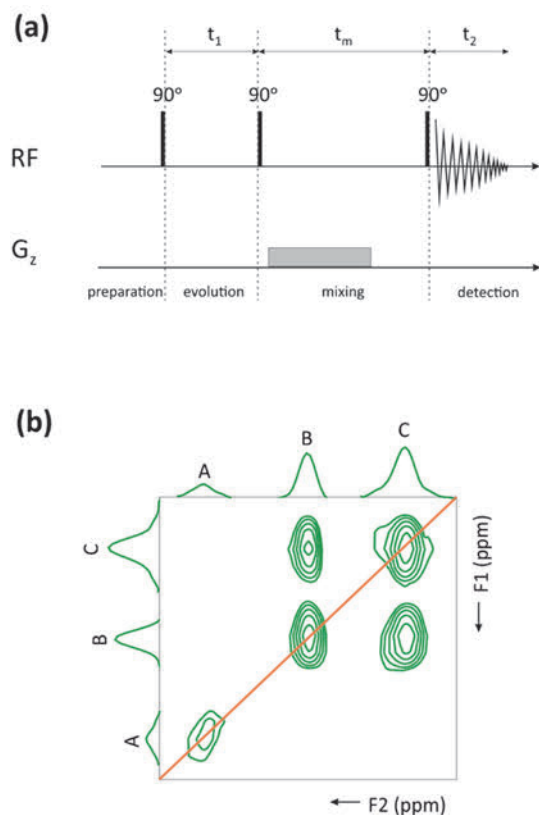
Fig. 10. (a) 2D EXSY pulse sequence and (b) the schematic of a 2D EXSY spectrum.

3.6.3 Selective inversion recovery

Selective IR experiment can be considered a 2D exchange experiment [111] (Fig. 11a). The pulse sequence for the selective IR experiment is similar to the IR experiment, but the 180° inversion pulse is a selective pulse, which only excites the selected frequency region (Fig. 11b). First, the selected peak (A) is inverted by the 180° pulse, and then the intensities of all the peaks are read by a 90° pulse after the recovery time t_d. If there is exchange between sites A and B, intensity of signal B is decreased as well due to selective inversion of A.

For a system undergoing exchange with n sites, the time dependence of the magnetizations is given by [112] (Fig. 11c)

44

$$\frac{\partial}{\partial t}\begin{pmatrix} M_1(t) - M_{1,\text{eq}} \\ M_2(t) - M_{2,\text{eq}} \\ \vdots \\ M_n(t) - M_{n,\text{eq}} \end{pmatrix} = -A \begin{pmatrix} M_1(t) - M_{1,eq} \\ M_2(t) - M_{2,eq} \\ \vdots \\ M_n(t) - M_{n,eq} \end{pmatrix}, \qquad (28)$$

where the $M_n(t)$ is the magnetization of the nth site at time t, and $M_{n,\text{eq}}$ is the equilibrium magnetization of site n. A is the magnetization decay rate matrix including the spin–lattice relaxation rates of site n ($R_{1,n}$) effecting the exchange rates between two sites n with m (k_{nm}):

$$A = \begin{pmatrix} R_{1,1} + k_{12} + \cdots + k_{1n} & -k_{21} & \cdots & -k_{n1} \\ -k_{12} & R_{1,2} + k_{21} + \cdots + k_{2n} & \cdots & -k_{n2} \\ \vdots & \vdots & \ddots & \vdots \\ -k_{1n} & -k_{2n} & \cdots & R_{1,n} + k_{n1} + \cdots + k_{nn} \end{pmatrix}. \quad (29)$$

The solution of the Eq. 28 can be written as

$$\begin{pmatrix} M_1(t) \\ M_2(t) \\ \vdots \\ M_n(t) \end{pmatrix} = \begin{pmatrix} M_{1,\text{eq}} \\ M_{2,\text{eq}} \\ \vdots \\ M_{n,\text{eq}} \end{pmatrix} + \exp(-At) \begin{pmatrix} M_1(0) - M_{1,\text{eq}} \\ M_2(0) - M_{2,\text{eq}} \\ \vdots \\ M_n(0) - M_{n,\text{eq}} \end{pmatrix}, \qquad (30)$$

where $M_n(0)$ is the initial magnetization right after the selective inversion.
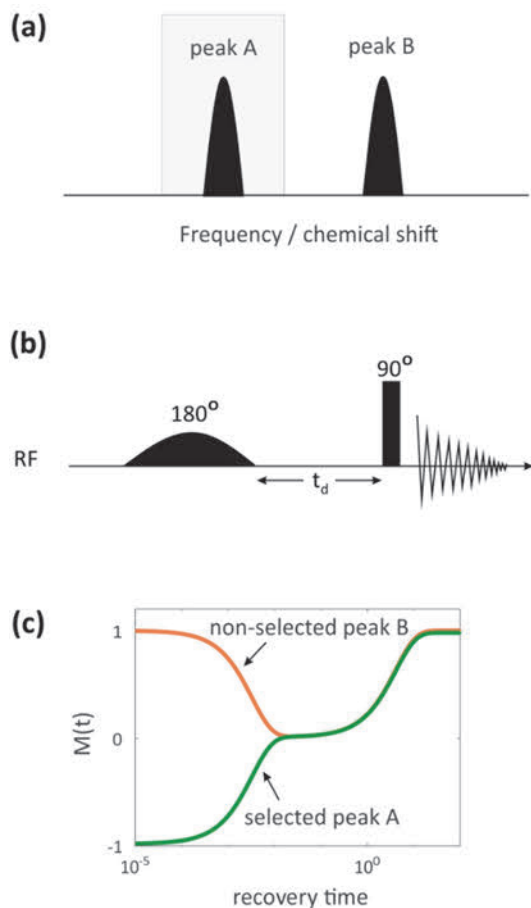
Fig. 11. (a) Schematic NMR spectra of a two-site system at equilibrium. (b) Selective IR pulse sequence. (c) Intensities of the two peaks as a function of recovery time in the selective IR experiment.

3.7   Single-sided NMR

Nowadays portable single-sided NMR devices are quickly becoming increasingly popular [113]. Unlike in the typical high-field spectrometer, the sample is outside of single-sided device (Fig. 12). Hence, the single-sided devices are not limited by the sample size. The unlimited sample size not only helps to recover the real production condition but also simplify the sample preparation for NMR scan. As the magnetic field of single-sided NMR devices is very inhomogeneous, the

46

frequency-domain chemical shifts cannot be acquired. However, time-domain experiments based on spin echoes, *i.e.*, relaxation and diffusion experiments, can be performed.

When performing a CPMG experiment on a single-sided device, the measured T_2 ($T_{2,\text{measured}}$) of the liquid in pores is affected by diffusion as [114]

$$\frac{1}{T_{2,\text{measured}}} = \frac{1}{T_{2,\text{real}}} + \frac{1}{3}\gamma^2 g^2 \tau^2 D, \tag{31}$$

To obtain the real T_2 values ($T_{2,\text{real}}$), $T_{2,\text{measured}}$ can be measured as a function of echo time 2τ so that $T_{2,\text{real}}$ and diffusion coefficient (D) can be separated. The effect of diffusion is negligible when D and g are small, and 2τ is short.

Fig. 12. Schematic of a single-sided NMR device. The curves with arrows represent the magnetic field lines, and "rf" refers to the radio frequency coil.

4 Pore structures and polymerization of geopolymers detected by ¹H and ¹²⁹Xe NMR

To get a better understanding of the pore structures of geopolymers, advanced NMR methods, including ¹H relaxometry, NMR cryoporometry, ¹²⁹Xe NMR, and relaxometry were applied. The pore sites, sizes, and connectivity of geopolymers were investigated bo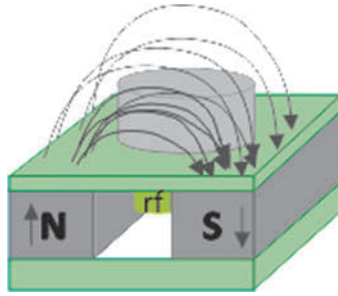th during and after curing. The effects of *w/s*, *Si/Al*, and NH₄OH posttreatment to the pore structure and geopolymerization, i.e., curing process, were also revealed.

N₂ physisorption and MIP were also used to get conventional data of pore structures of the geopolymers to compare with NMR data. ²⁷Al and ²⁹Si MAS SSNMR were collected to characterize the chemical structures.

4.1 Pore structure during and after the curing process detected by ¹H NMR relaxometry and cryoporometry (Paper I)

The ¹H NMR relaxometry is an efficient tool for detecting the pore sizes and connectivity in cementitious materials in a noninvasive and nondestructive manner [15]. The ¹H NMR cryoporometry is also a noninvasive method, in which the pore space is probed by observing phase transitions of water confined in pores to acquire PSD [17].

In Paper I, three geopolymers, G0.66, G0.63, and G0.53, were prepared. They had the *w/s* of 0.66, 0.63, and 0.59, respectively, and oxide molar ratios of SiO_2: Al_2O_3: Na_2O: H_2O = 4: 1: 1: X, where X = 17, 16, and 15, respectively. We applied relaxometry methods to longitudinally monitor the change in their pore network during curing. 2D T_1–T_2 and T_2–T_2 maps were used to detect the pore connectivity, and NMR cryoporometry was applied to detect the PSDs of cured geopolymers. Additionally, the effects of the *w/s* ratio on both curing process and cured pore structure were investigated.

4.1.1 Monitoring of curing process

The curing processes of three geopolymers with different *w/s* were monitored by acquiring T_2 and T_1 data on the Magritek Spinsolve 43 MHz NMR spectrometer. The inherent residual water in the system can be exploited as an NMR probe [115,116]. The relaxometry data was fit using Eqs. 13 and 12 (Figs. 13a–c and 14a–c) to find the relaxation times. The T_2 and T_1 distributions at various curing times

are plotted in Figs. 13d–f and 14d–f. The T_2 and T_1 plots as a function of curing time are shown in Figs. 13g and 14g. The S_0 fitted from T_2 and T_1 data are shown in Figs. 13h–i and 14h–i. The S_0 is equal to $M_{xy}(0)$ in Eq. 13 or $M_{z,eq}$ in Eq. 12.

For the porous systems, the measured T_2 and T_1 values are related to the pore size according to Eq. 14. As shown in Figs. 13g and 14g, the T_2 and T_1 values decrease until day 8 and then remain stable until day 14 for all three samples. The decreasing T_2 and T_1 values during the first 8 days of curing are ascribed to the decreasing pore diameter as a function of curing time, which indicates that pore structures were gradually forming. All three samples finished their curing process at day 8.

The S_0 values acquired from T_2 and T_1 data represent the mobile proton signal intensities. The S_0 starts from a value smaller than the second point. This low starting point indicates water was adsorbed to participate the chemical reaction of the dissolution of metakaolin and the dissolution stage is assumed to occur before the data were collected. From hours 1 to 5, S_0 increased for three geopolymers (Figs. 13i and 14i), and this is ascribed to the water released during the hydration stage [34]. The detectable water content then decreased until day 8 because, as the curing proceeds, the free water becomes bound water, and the bound water is silent in NMR experiments due to its short T_2 [117]. At this time point, the signal intensity decreases as the *w/s* ratio decreases.

50
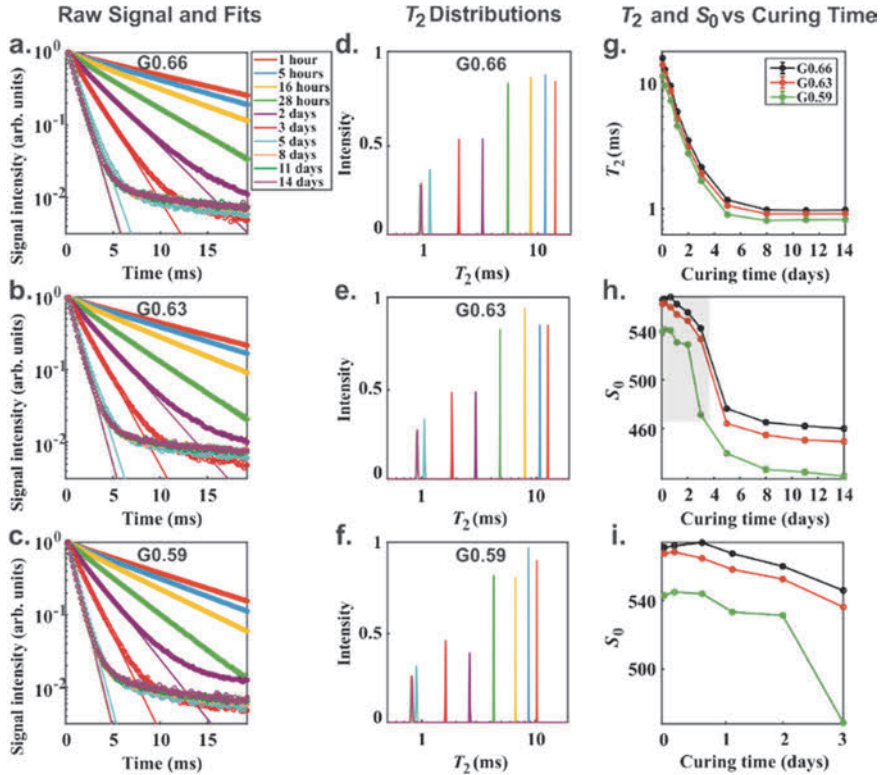
Fig. 13. T_2 derived from CPMG experiments during curing of three geopolymers: G0.66, G0.63, and G0.59. In a–f, the curing time is color coded. (a–c) raw and fitted signal of CPMG experiments, (d–f) T_2 distributions derived from the signal. (g) T_2 as a function of curing time and (h,i) S_0 as a function of curing time (Reprinted under CC BY 4.0 license from Paper I © 2021 Authors).
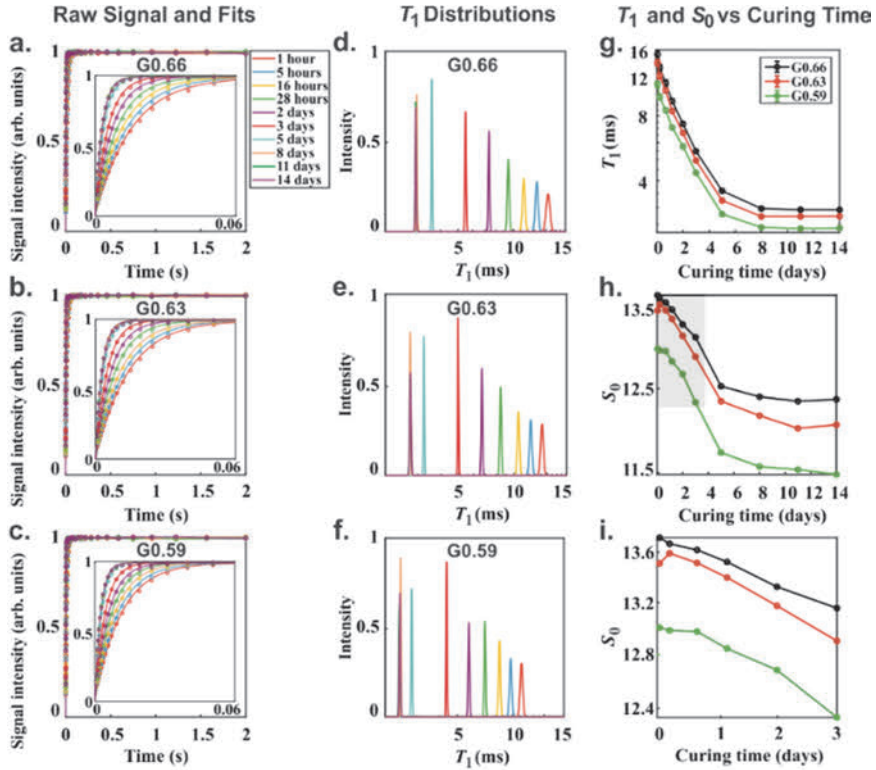
Fig. 14. T_1 results derived from T_1SR experiments during curing of three geopolymers: G0.66, G0.63, and G0.59. (a–c) raw and fitted signal of T_1SR experiments, (d–f) T_1 distributions derived from the signal, (g) T_1 as a function of curing time, and (h,i) S_0 as a function of curing time (Reprinted under CC BY 4.0 license from Paper I © 2021 Authors).

4.1.2 Pore sites and connectivity of cured geopolymers

After 14 days of curing, three samples were saturated with water for 8 days. After 8 days of saturation, the samples were fully water-saturated, as the signal intensities did not increase anymore. 2D T_1–T_2 and T_2–T_2 experiments were then used to detect the matured pore structures of the three geopolymers on the Magritek Spinsolve 43 MHz NMR spectrometer. Four peaks are present in the T_1–T_2 correlation maps (Figs. 15 a–c), and three peaks are present in the T_2–T_2 exchange maps (Figs. 15 d–f). In the T_1–T_2 correlation maps, there are three peaks along the line of $T_1 = 3.7T_2$. These peaks are ascribed to three pores with three pore diameters. The peak with

52

long T_2 and T_1 is the pore with a large pore diameter. Peaks I, II, and III are attributed to water in pores with small, medium, and large pore diameters. An exchange peak is present between the peaks representing water in small and medium pores. This means that small and medium pores are well connected, i.e., water moves between the two pores. In the T_2–T_2 exchange spectra, the three pores are also detected. The peak of the small pores is missing from diagonal because it was filtered by the 1 ms storage time. However, the exchange peak between the missing Peaks I and II still appears.
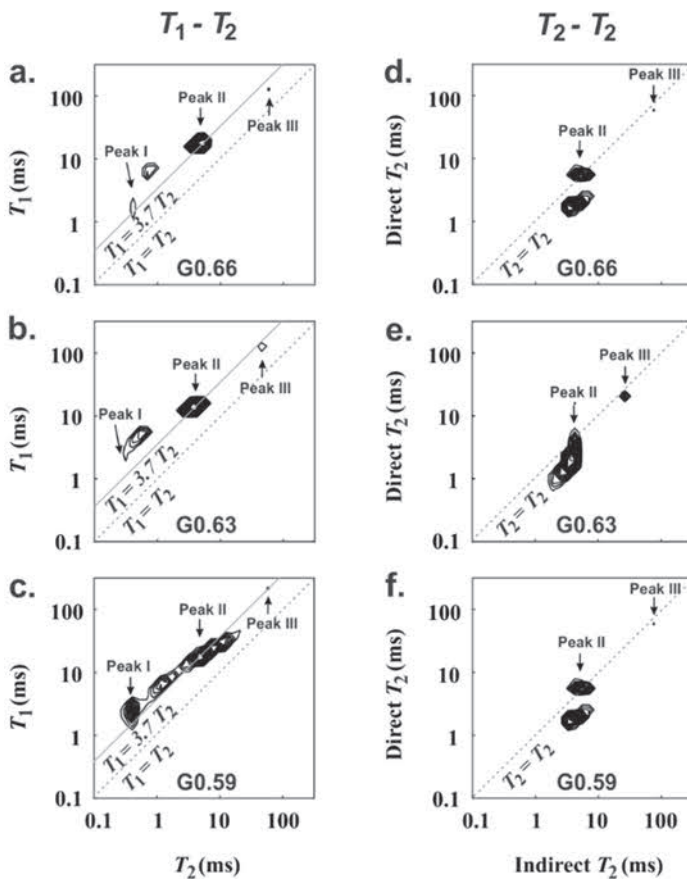
Fig. 15. (a–c) T_1–T_2 correlation maps and (d–f) T_2–T_2 exchange spectra acquired with mixing time of 1 ms of G0.66, G0.63, and G0.59 samples (Reprinted under CC BY 4.0 license from Paper I © 2021 Authors).

4.1.3 Pore size distributions of cured geopolymers

To obtain the PSDs, the NMR cryoporometry experiments were performed with three different echo times on Bruker Avance III 500 MHz spectrometer. When the longer echo time is used, lower signal intensities are obtained due to T_2 filtering (Figs. 16a–c). The intensities of pores A and B decrease more than pore C. This implies that pores A and B have shorter T_2 than pore C, and thus the pores A, B, and C correspond to the peaks I, II, and III in the 2D spectra, respectively (Fig. 15).
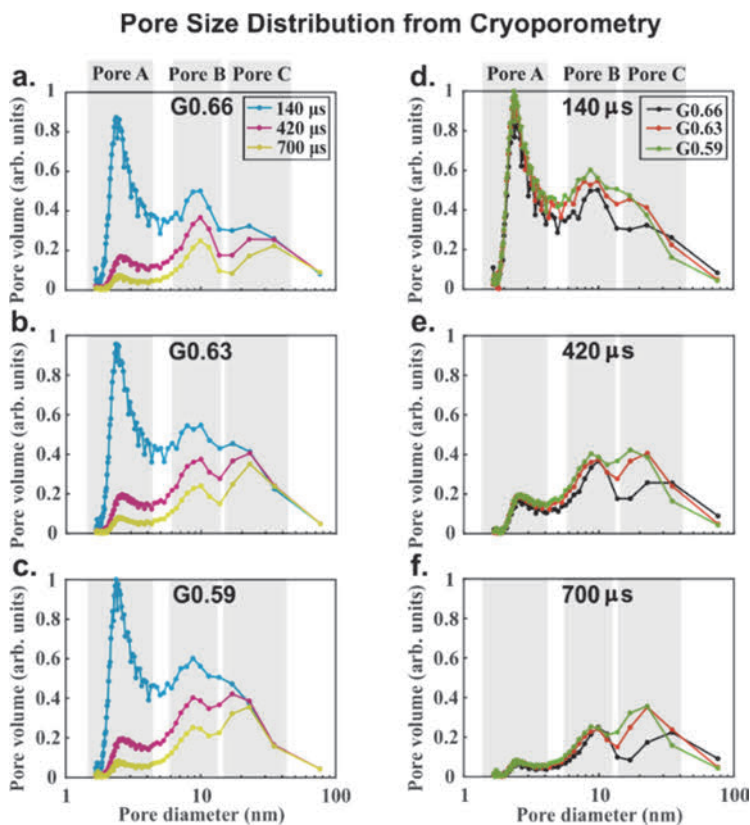
Fig. 16. PSDs derived from NMR cryoporometry experiments with different echo times (Reprinted under CC BY 4.0 license from Paper I © 2021 Authors).

The results of the NMR cryoporometry experiments with the shortest echo time are compared with the PSDs acquired by two conventional methods, N_2 physisorption and MIP (Fig. 17). Three mesopores around 3, 10, and 30 nm were detected using

both cryoporometry and N_2 physisorption. The pore diameters measured by these two methods are consistent with each other (Table 1). However, only one peak is shown in MIP plots, because MIP measured the size of the pore throats instead of the pore bodies or smallest pores are under the MIP detection limit. The pore sizes of medium (B) and large (C) pores are found to decrease as the *w/s* decreases (Table 1), but the pore size of small pores (S) does not change with *w/s* changing.
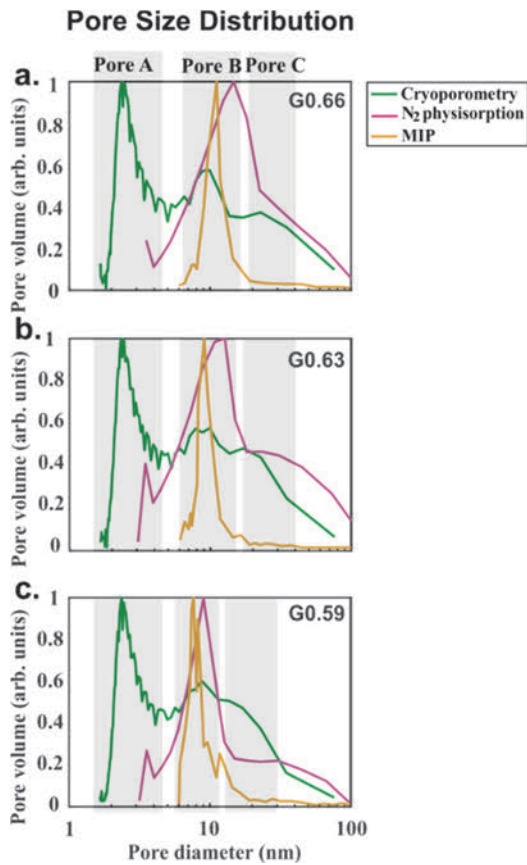
Fig. 17. PSDs measured using cryoporometry, N_2 physisorption, and MIP of (a) G0.66, (b) G0.63 and (c) G0.59 (Reprinted under CC BY 4.0 license from Paper I © 2021 Authors).

Table 1. Pore diameters measured using three methods. The location of the maxima of the peaks is shown (Adapted under CC BY 4.0 license from Paper I © 2021 Authors).

Pore diameter (nm)	Cryoporometry			N_2 physisorption			MIP		
	A	B	C	A	B	C	A	B	C
G 0.66	2.4	9.9	35	3.5	15	42	–	11	–
G 0.63	2.5	9.9	23	3.5	11	31	–	9.1	–
G 0.59	2.5	8.8	17	3.6	9.0	30	–	7.7	–

Three pores with different pore sizes were found in the three geopolymers with the *w/s* of 0.66, 063, and 0.59 (Fig. 18), respectively. The small pores with a pore size of about 3 nm were hypothesized to be zeolite-analogous pores, and their sizes do not change. Zeolite-analogous pores of geopolymer were assumed to result from the analogous building unit cells shown in zeolites because this pore size is consistent with the unit cell size of zeolite Y [118]. The medium pores with the pore size of 9 nm were hypothesized to arise from disordered arrangement of the unit cells, which is called a geopolymer disordered pore. The large pores are believed to be defective sites, stemming from the presence of the terminal hydroxyls resulting from the breakage of -Si-O-Al- bonds.
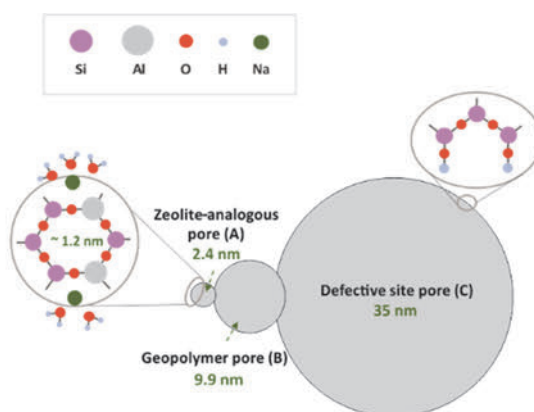
Fig. 18. Schematic of the cured pore structure of geopolymer (Adapted under CC BY 4.0 license from Paper I © 2021 Authors).

In this work, the growth of the pore structure was longitudinally monitored by the change in T_2 and T_1 values, and the matured pore structures were studied by 2D relaxometry, as well as NMR cryoporometry. Three mesopores were found, from which the two small pores were found to be connected. The two larger mesopores

were found to have a slightly increasing pore size with an increasing *w/s*. A range of *w/s* was hypothesized to be the reason for the small change of pore size.

4.2   Effect of *w/s* on the pore structure detected by ^{129}Xe NMR (Paper II)

In Paper I, the two smaller mesopores of geopolymers were found to be connected. In Paper II, the level of pore connectivity was further explored. Additionally, the pore structures of the geopolymers with a narrow range of the *w/s* 0.66–0.59 was studied in Paper I. In Paper II, a wider *w/s* range of 0.75–0.42 was studied by ^{129}Xe NMR methods on Bruker Avance III 400 and 600 MHz spectrometers. Six samples were prepared with *w/s* ratios of 0.75, 0.66, 0.63, 0.59, 0.50, and 0.42, respectively. They had oxide molar ratios: SiO_2: Al_2O_3: Na_2O: H_2O = 4: 1: 1: X, where X = 19, 17, 16, 15, 13, and 11, respectively.

4.2.1 Pore sites

The ^{129}Xe NMR chemical shift is highly sensitive to the local chemical and physical environment. In porous materials, the ^{129}Xe NMR chemical shift is sensitive to pore sizes: the smaller the pore, the larger the shift [119].

The ^{129}Xe NMR spectra measured at room temperature for six geopolymers with different *w/s* are shown in Fig. 19. Two peaks and pore sites are found in G0.75 and G0.42 (Figs. 19a and 19f), while three pore sites are found in the other samples with medium water content (Figs. 19b–e). All the samples show one peak around 2 ppm, which is ascribed to Xe in large pores or free gas between the particles. This peak is labeled F. G0.75 and G0.42 have another peak around 14 ppm, and this is assigned as a big pore, named B. However, the B signal intensity of G0.42 is low, and this indicates that the pore structure of G0.42 did not form well. This is reasonable because the *w/s* = 0.42 is theoretically the lowest *w/s* for synthesizing a geopolymer. The four medium water content samples have larger chemical shifts, shown at about 30 ppm, and thereby smaller pore sizes for pore B than G0.75 and G0.42. Additionally, a small pore signal S is found for G0.66 to G0.50 at around 56 ppm.
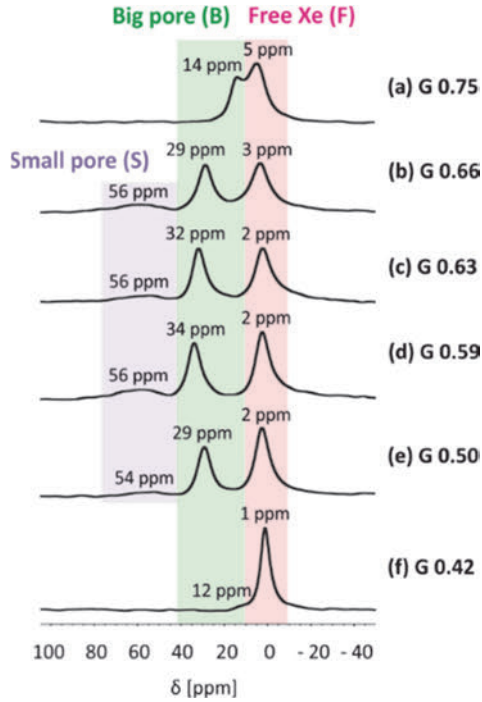
Fig. 19. ^{129}Xe spectra of Xe gas adsorbed in six geopolymers (Reprinted under CC BY 4.0 license from Paper II © 2022 Authors).

4.2.2 Mesopore size measurements by variable temperature experiments

To measure the pore sizes associated with these peaks, VT (182–302 K), the ^{129}Xe NMR experiments were performed (Fig. 20a). The pore size of B pores was obtained by fitting Eq. 26 with the chemical shifts of peak B as a function of temperature (Fig. 20b). The resulting pore sizes were plotted and compared with the average pore sizes measured by N_2 physisorption in Fig. 20c. It should be noted is that the PSDs derived from N_2 physisorption show three mesopores: B1, B2, and B3, while these three pores average together in the ^{129}Xe spectra as one peak B. The pore sizes acquired from the two methods are in close agreement with each other, and the deviation is <7% (Fig. 20d). For G0.50–G0.66, the average pore size decreases as the *w/s* decreases, agreeing with the N_2 physisorption results. Although G0.75 shows a pore size of 35 nm from N_2 physisorption data, the VT ^{129}Xe NMR

58

data show that it has the pore size of about 213 nm. It is hypothesized that the average pore size of G0.75 is greater than the upper detection limit of the N_2 physisorption measurement here. The fitting results also include the heats of Xe gas adsorption (Fig. 20e). The G0.75 sample has higher heat of adsorption than other samples. This means the Xe gas is more stable in G0.75 than in other samples.
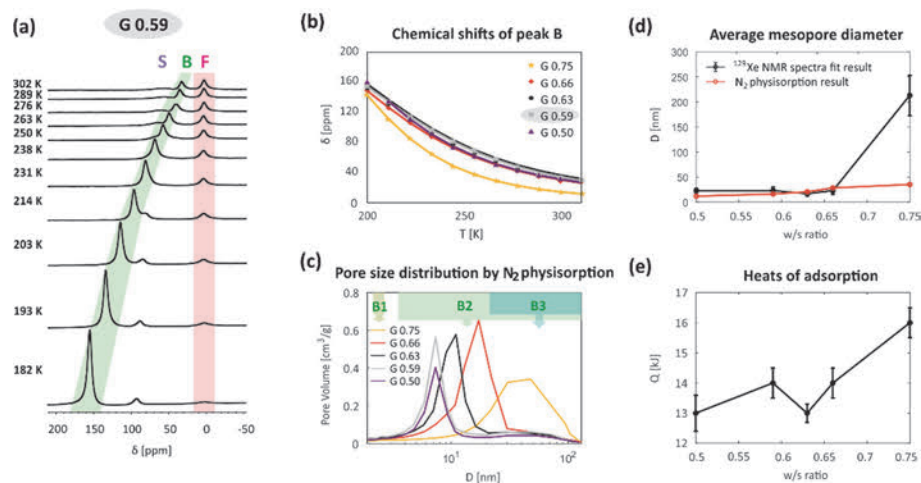
Fig. 20. (a) VT ^{129}Xe spectra and (b) ^{129}Xe chemical shifts (dots) determined from the VT ^{129}Xe spectra and fitted lines as a function of temperature, (c) PSD acquired from N_2 physisorption, (d) average pore size of pore B from two methods, and (e) the fitted heats of adsorption extracted from VT ^{129}Xe data of five geopolymers with *w/s* of 0.75, 0.66, 0.63, 0.59, and 0.50 (Reprinted under CC BY 4.0 license from Paper II © 2022 Authors).

4.2.3 Pore connectivity detected by selective inversion recovery and relaxation

The selective IR ^{129}Xe NMR experiments were performed to quantify the exchange rates at 188 K and 263 K. The signal intensities of B, F, and S as a function of recovery time at 188 K are plotted in Fig. 21c. The intensity of peak F starts to decrease after B is inverted in the period of 1–10 ms, and this is due to the magnetization transfer. The exchange rates k_{BF} were found by fitting Eq. 30 with the signal intensity as a function of inversion time (Fig. 21e). At 188 K, k_{BF} is equal to 20 s^{-1} for G0.66–0.50. Corresponding exchange rates for G0.75 and G0.42 could not be determined due to a low signal-to-noise ratio. At 263 K, k_{BF} is about 100 s^{-1}

for G0.63 to G0.50 (Fig. 21f). When w/s increases, k_{BF} increases to 160 s^{-1} and 230 s^{-1} for G0.66 and G 0.75, respectively.
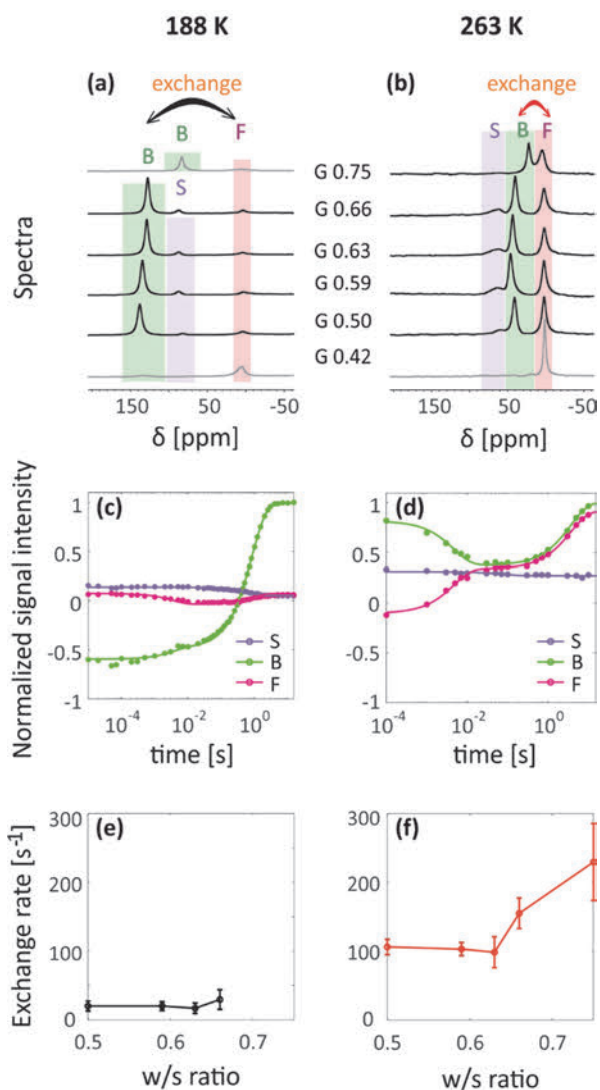
Fig. 21. Exchange results acquired from selective IR ^{129}**Xe NMR experiments at (a, c, and e) 188 K and (b, d, and f) 263 K. (a,b)** ^{129}**Xe spectra, (c,d) plots of signal intensity as a function of recovery time and (e,f) plots of exchange rates as a function of** *w/s* **at two temperatures (Adapted under CC BY 4.0 license from Paper II © 2022 Authors).**

T_1 is plotted as a function of w/s in Fig. 22. At 188 K, T_1 of F and B are equal (Fig. 22c). This is because the exchange between these sites is faster than the T_1 relaxation of the respective sites, $k_{BF}^{-1} \ll T_1$. S has $T_1$ of about half of that for F and B, indicating that exchange times t_{SF} and t_{SB} are equal or longer than T_1, i.e., t_{SF} and $t_{SB} \geq 0.5$ s. The exchange rates between S and other sites were not detected or studied here due to the small size of peak S. Additionally, T_1 of all the signals decreases as w/s increases. At 263 K, the faster exchange and longer T_1 leads to more obvious exchange averaging, reflected by almost the same T_1 values for all three sites (Fig. 22d). Exchange rates k_{SF}^{-1} and k_{SB}^{-1} are thereby <4 s. In conclusion, the exchange times between S and other two sites are in the order of seconds.

The T_2 of F and B as a function of w/s is also plotted in Fig. 22. The T_2 values of S were not detected as the signal intensities are too low. At 188 K (Fig. 22a), the T_2 of F (0.2 ms) is much shorter than the T_2 of B (1–3 ms), which means T_2 is not exchange averaged as T_2 is shorter than exchange time k_{BF}^{-1} (50 ms). The T_2 of B increases with increasing w/s, suggesting that the mesopore size increases with an increasing w/s, which agrees with the average pore diameters measured by N_2 physisorption (Figs. 20c and 20d). At 263 K, the T_2 values of F and B are closer to each other, because of the averaging from fast exchange (Fig. 22b).
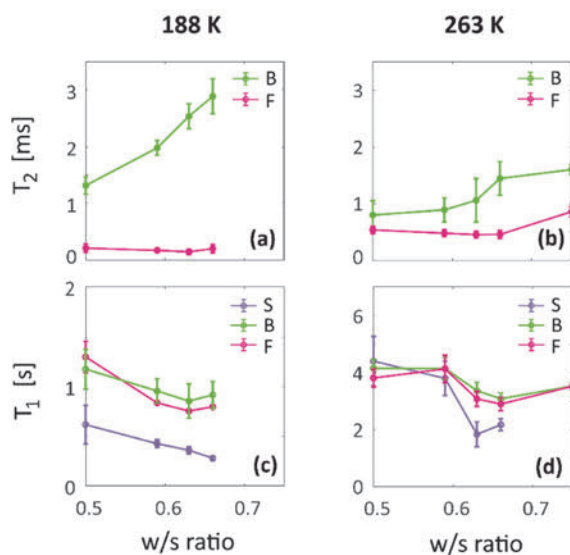

Fig. 22. ^{129}Xe T_2 and T_1 as a function of w/s at 188 and 263 K (Reprinted under CC BY 4.0 license from Paper II © 2022 Authors).

The ^{129}Xe gas NMR methods were applied in this thesis to study the pore sites, sizes, and connectivity, while liquid-state ^{1}H NMR methods were applied in Paper I. Furthermore, in Paper II, a wider *w/s* range was studied than in Paper I. Three pore sites were identified when *w/s* was in the range of 0.63–0.50. When the *w/s* increased to 0.75, just two pore sites were formed and the lowest *w/s* of 0.42 did not form a good pore structure. The ^{1}H relaxometry showed that the small pores are connected to the medium pores, while ^{129}Xe NMR indicated that all detected pores were connected (Fig. 23). Together, these two papers reveal that when *w/s* increases, larger mesopores are formed. The ^{129}Xe NMR also revealed that when *w/s* increased up to 0.66, the pore connectivity was enhanced.
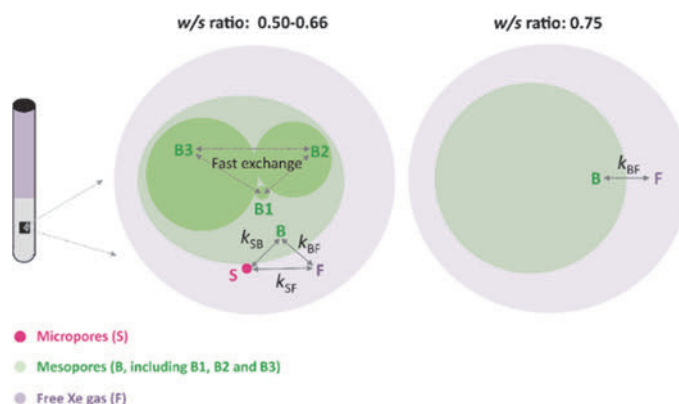
Fig. 23. Schematic of pore structures of geopolymers detected using the ^{129}Xe NMR methods (Adapted under CC BY 4.0 license from Paper II © 2022 Authors).

4.3 Effect of *Si/Al* on geopolymerization studied by a single-sided NMR device (Paper III)

The effects of *w/s* on the curing process and pore structure were thoroughly studied by ^{1}H relaxometry, cryoporometry, as well as ^{129}Xe spectroscopy and relaxometry. The effect of another factor, *Si/Al*, to the mechanism of geopolymerization and pore structure was also investigated. Four samples with various *Si/Al* of 1, 1.5, 2, and 2.5 were prepared and named G1, G1.5, G2, and G2.5, respectively. Four samples had oxide molar ratios of $Na_2O: H_2O: Al_2O_3: SiO_2 = 1: 17: 1: X$, where X = 2, 3, 4, 5, respectively. They all have a diameter of 5.1 cm and a height of 1.5 cm.

A small size of the specimen used for normal NMR device was suspected to be unable to recover the real state of geopolymer. In Paper III, a single-sided NMR

device (Fig. 12) with 13.29 MHz operating frequency and 7 T/m (310 kHz/mm) constant gradient was used to perform NMR experiments. The measurements by this device were not constrained by the sample size.

4.3.1 Geopolymerization processes

The curing process was monitored by T_2 and T_1 measurements for four geopolymers with different Si/Al (G1, G1.5, G2, and G2.5). G1 showed five stages of geopolymerization, while G1.5, G2, and G2.5 showed three stages.

In G1 (Fig. 24), S_0 starts from a low signal intensity, which provides indirect evidence of the dissolution of metakaolin before the data collection. When metakaolin is dissolved into Si and Al monomers, water is consumed in the dissolution reaction [34]. This low S_0 starting point was also found in Paper I (Figs. 13i and 14i).

The first 3 hours of measurement comprise the second stage of geopolymerization, during which the adsorbed water is released, shown as an increase of S_0. This stage is a gelation stage [120], where the monomers gradually form to a gel phase with Si/Al of 1, gel 1. The decreased T_2 indicates decreased pore size and means that the pore structure has gradually formed.

After hour 3, T_2 and S_0 decrease until hour 12. The decreased S_0 is attributed to water binding with gel 1. The bound water could not be detected in NMR experiments. The bound water occupies pore spaces and leads to the decreased T_2.

From hour 12 to day 13, the T_2 increases, and S_0 is stable. This is the fourth stage, a reorganization stage. During the reorganization, the gel phase transforms from gel 1 with Si/Al of 1 to gel 2 with Si/Al of 2. Gel 2 has a larger pore size than gel 1 and thus T_2 increases. S_0 is constant due to two opposite effects: Water is released during reorganization and then bound to the solid matrix. T_1/T_2 increases during the stage IV, which suggests that gel 2 has higher surface affinity to water than gel 1 (see Section 3.3.4).

During the last stage, from day 13 to day 33, T_2 decreases, and S_0 increases. Gel 2 including bound water polymerizes and condenses to form the final geopolymer skeleton, which results in decreased T_2. This stage is the polymerization and condensation stage, where water is released. G1 finished its curing in 33 days. Although S_0 still decreased slightly by 11% over the next 84 days, this was assumed to be a consequence of the evaporation of water.
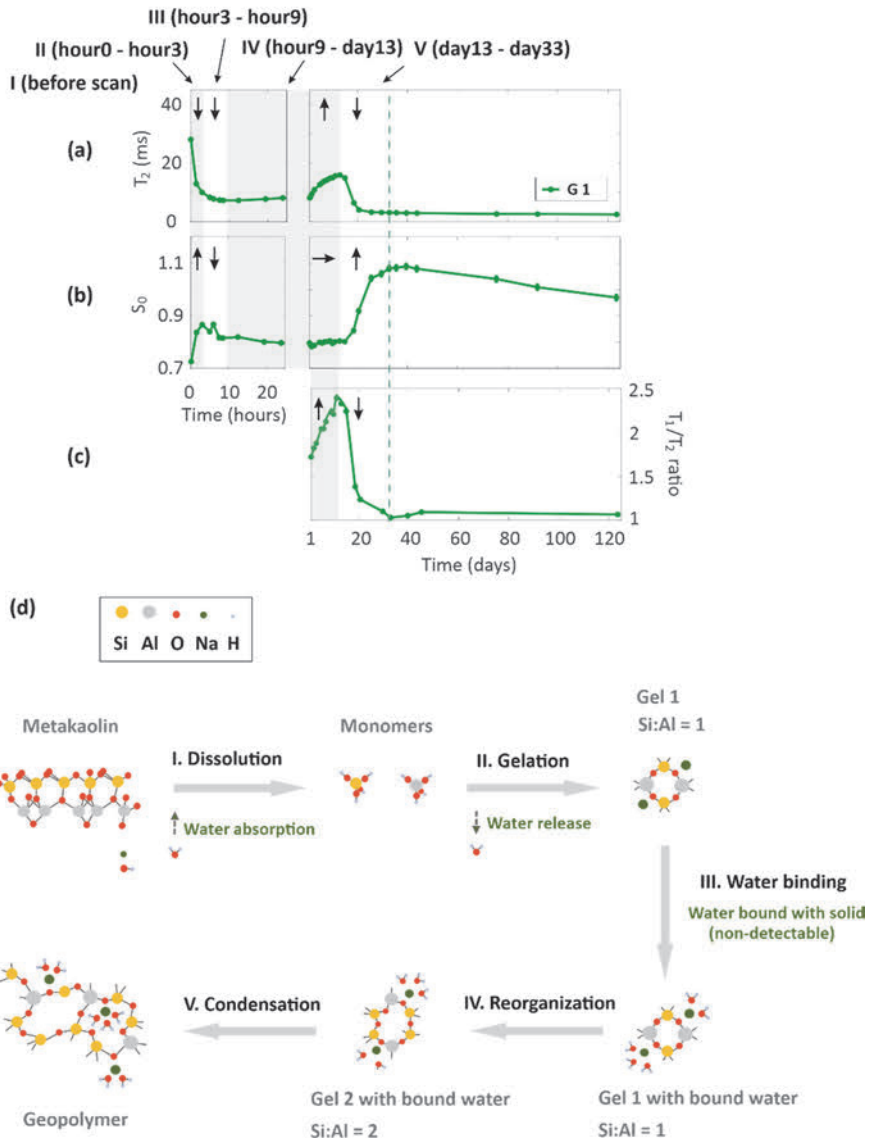
Fig. 24. (a) T_2, (b) S_0 and (c) T_1/T_2 data of G1 as a function of curing time, as well as (d) the schematic figure of geopolymerization of G1 (Reprinted, with permission, from Paper III © 2022 Authors).

In G1.5, G2, and G2.5 (Fig. 25), the same low starting point of S_0 is also observed, indicating the dissolution stage before the experiments. The first hour is the second stage, gelation stage, where T_2 decreases and S_0 increases. These three samples are different from G1: After the gelation stage, the gel phase with *Si/Al* of 2 is formed directly. This results from one of two mechanisms: 1) the different ratio of Si with Al monomers during dissolution or 2) gel 1 is too short lived to be observed with this experimental set up. The third stage, the condensation stage, finishes at day 5, day 10, and day 124 for G1.5, G2, and G2.5, respectively. Both T_2 and S_0 decrease during this last stage. By comparing these three samples, we found that the lower *Si/Al* contributes to a shorter curing process, with a shorter condensation stage. T_1/T_2 for samples G1.5 and G2 do not change significantly during the observation period, most probably because most of the chemical reactions has already taken place before the first observation point on day 1. In contrast, T_1/T_2 of G2.5 increased until the end of monitoring. G2.5 has the lowest *w/s* of 2.4. Therefore, we interpret that the low amount of water is limiting the progress of polymerization reaction in the G2.5 sample.
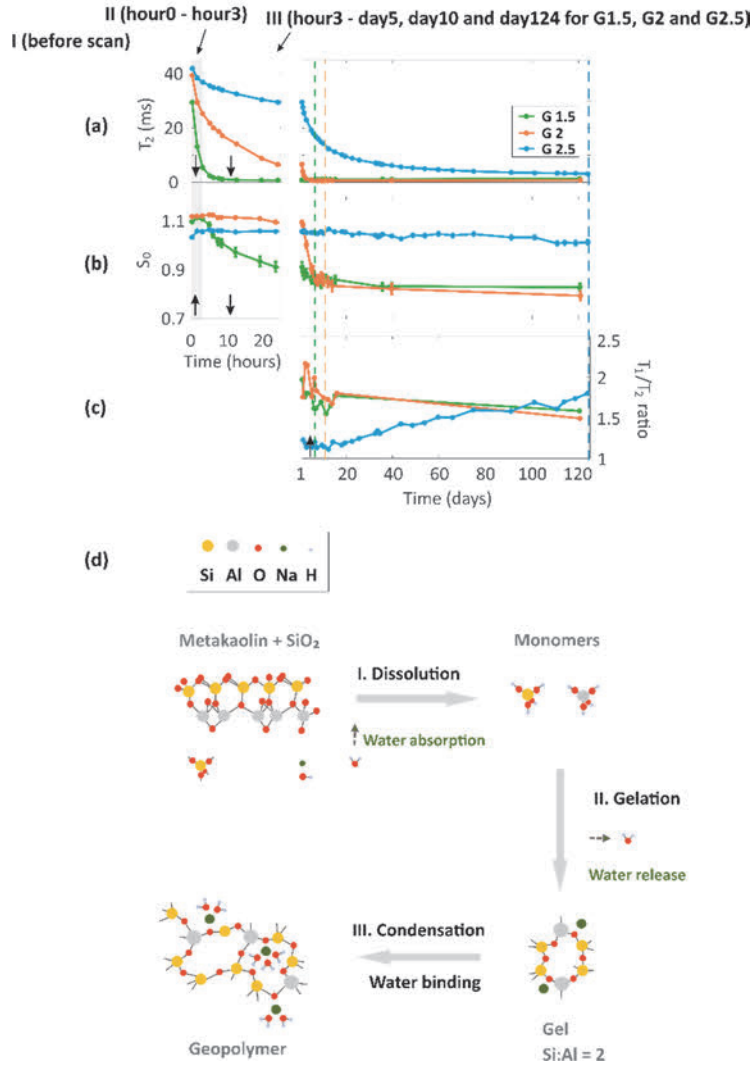
Fig. 25. (a) T_2, (b) S_0, and (c) T_1/T_2 data of G1.5, G2, and G2.5 as a function of curing time and (d) their schematic of geopolymerization (Reprinted, with permission, from Paper III © 2022 Authors).

66

4.3.2 Chemical and pore structures of cured geopolymers

The effect of *Si/Al* on the chemical and pore structures was characterized after curing. The chemical structure was studied by ^{27}Al MAS SSNMR on the Bruker Avance III 300 MHz spectrometer. N_2 physisorption, T_2, and analysis T_1/T_2 were used to measure the pore sizes and surface affinity to water.

The ^{27}Al MAS SSNMR spectra show two peaks for all four geopolymers (Fig. 26). The peak at 58 ppm arises from tetracoordinate Al [121], which is structural Al, while the peak at 10 ppm is hexacoordinate Al from unreacted metakaolin [121]. In the case of the three samples with *Si/Al* < 2.5, the unreacted metakaolin peak is very small, but it is quite large for the G2.5 sample. This means that metakaolin did not fully dissolve in the NaOH solution when *Si/Al* was 2.5.
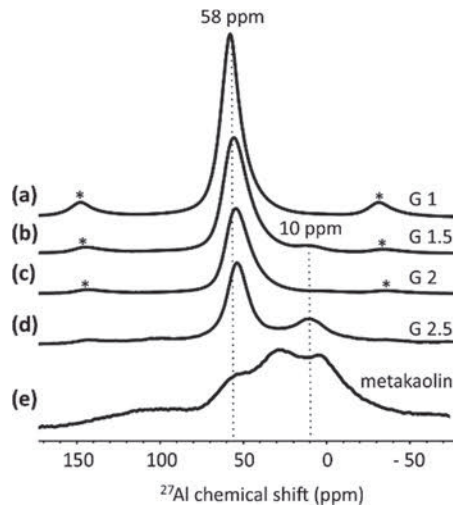
Fig. 26. ^{27}Al MAS SSNMR spectra of (a) G1, (b) G1.5, (c) G2, (d) G2.5, and (e) metakaolin used for synthesizing geopolymers (Reprinted, with permission, from Paper III © 2022 Authors).

According to the N_2 physisorption analysis, pore size decreases as *Si/Al* increases for G1 (48.2 nm), G1.5 (28.7 nm), and G2 (21.1 nm) samples (Fig. 27). This is in compliance with previous studies, which showed that larger *Si/Al* leads to smaller pore diameters in the *Si/Al* range of 1 to 2 [122]. Additionally, G1 has a peak at about 2.6 nm (conversed from the increasement from 0.45 to 0.55 P/P_0 on the N_2 desorption curve), which is attributed to zeolite-analogous pores [123, 124]. This is in agreement with the finding that the geopolymer synthesized from raw material

with *Si/Al* of 1 prefers to form zeolite phase [125]. Therefore, we hypothesize that the presence of two gel phases during geopolymerization leads to the growth of zeolite phase and zeolite-analog pores. T_2 values decrease with increasing *Si/Al* due to decreased pore size.
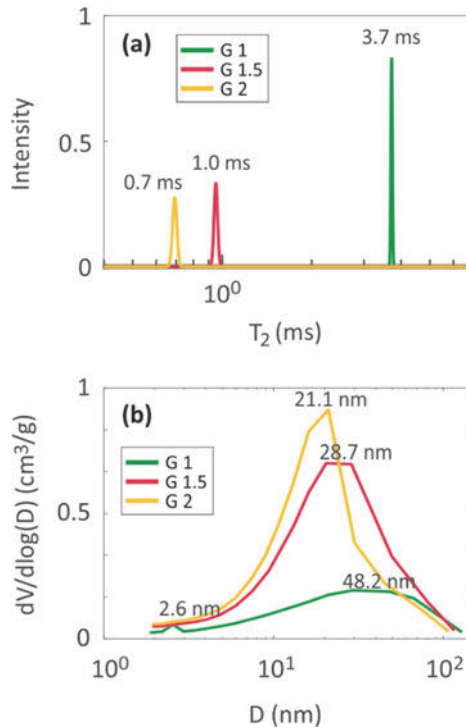
Fig. 27. (a) T_2 **distributions and (b) PSD from** N_2 **physisorption of G1, G1.5, and G2 (Reprinted, with permission, from Paper III © 2022 Authors).**

The surface affinity is related to some other important properties of geopolymers, such as structural stability when they are used as fire-resistant materials and the ability of water adsorption when they are used as coating materials. T_1/T_2 has been stated in Section 3.3.4 to represents the surface affinity of porous materials to water. According to Fig. 28, T_1/T_2 is the highest (2.3) when *Si/Al* is 1.5. This indicates that G1.5 has the highest ability to adsorb water, making it the most promising candidate for fire-resistant and water-adsorption material applications.
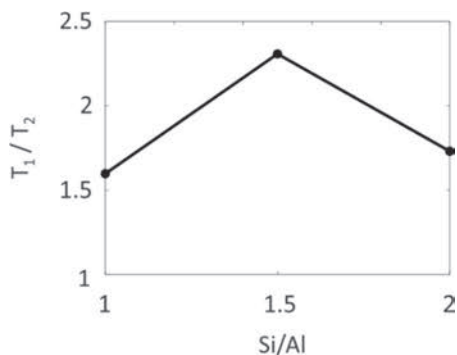
Fig. 28. T_1/ T_2 **as a function of** *Si/Al* **in the range of 1–2 (Reprinted, with permission, from Paper III © 2022 Authors).**

In summary, by monitoring the curing process with T_2 measurements on NMR-MOUSE, the *Si/Al* was found to affect geopolymerization. The sample with low *Si/Al* showed two gel phases during geopolymerization, while only one gel phase was observed for G1.5–2.5. The presence of two gel phases was also assumed to result in the formation of zeolite phase in geopolymer.

4.4 Effect of NH₄OH posttreatment on pore structure of geopolymer detected by ¹²⁹Xe and ¹H NMR (Paper IV)

In Papers I–III, the effects of *w/s* and *Si/Al* on the pore structure were studied by ^{1}H and ^{129}Xe NMR methods. In Paper IV, the effect of NH₄OH treatment on the pore structure of geopolymer powders was investigated, which has not been studied earlier. With this work, the development of a new way for tailoring the pore structure of geopolymer was investigated.

Four sets of same geopolymer powders with oxide molar ratios of Na_2O: Al_2O_3: SiO_2: H_2O = 1: 1.2: 3.8: 13.6 were treated with various NH₄OH treatment times under room temperature, i.e., 0 min, 15 min, 3 h, and 24 h. They were named N1, N2, N3, and N4, respectively. ^{129}Xe NMR experiments were conducted on Bruker Avance III 300 and 600 MHz spectrometers. ^{1}H relaxation experiments were performed on Magritek Spinsolve 43 MHz NMR spectrometer, and ^{1}H NMR cryoporometry experiments were performed on Bruker Avance III 500 MHz spectrometer.

4.4.1 Pore accessibility

The pore accessibility of the four samples, N1, N2, N3, and N4, were probed by inserted Xe gas. ^{129}Xe spectra and dynamics were studied: ^{129}Xe exchange rates, T_1 and T_2 were measured by performing selective IR, IR, and CPMG experiments, respectively.

Two peaks were visible in the ^{129}Xe spectra for the first three samples with the NH$_4$OH treatment time from 0 to 3 hours (Figs. 29a–c). One peak appears at 6.6 ppm, and it is attributed to the gas between particles, named BP. There is also a peak at around 45 ppm attributed to the gas inside particles, named inside pore (IP). The differences of chemical shifts between these three samples is slight. When the geopolymer was treated by NH$_4$OH for 24 h (Fig. 29d), the spectrum shows only a broad peak at 19.9 ppm. This is a consequence of accelerated exchange due to the smaller particle size of sample N4 compared to other samples (Fig. 30a), which leads to exchange averaging of IP and BP signals [126].

As shown in the plots of exchange rates between inside (IP) and outside (BP) pores (Fig. 29e), the exchange rates are in the range of 140–270 s^{-1}. Like the two sites detected in Paper II (Figs. 21 and 22), T_1 is the same (Fig. 29f), but T_2 values are different (Fig. 29c) for IP and BP for these three samples. This is because the exchange is faster than T_1: k (140 to 270 s^{-1}) $\gg$ 1/T_1 (0.33 to 0.67 s^{-1}) that T_1 of two sites are exchange averaged.

There is no change of exchange rates between the three samples, which means that the pore accessibility for guest gas does not change when the NH$_4$OH treatment time is no more than 3 h. N1 has a shorter T_1 (1.5 s) than N2 and N3 (3 s). Increase of T_1 of IP and BP after the NH$_4$OH treatment is assumed to arise from the changing chemical environment: NH$_4^+$ gradually exchange with the original cations, like Na$^+$ and H$^+$, in the pores. T_2 do not change as a function of treatment time (in 3 h).

By using ^{129}Xe NMR methods, the inside pores of four samples are found to be accessible for all four samples, as illustrated in Figs. 30b and 30c.
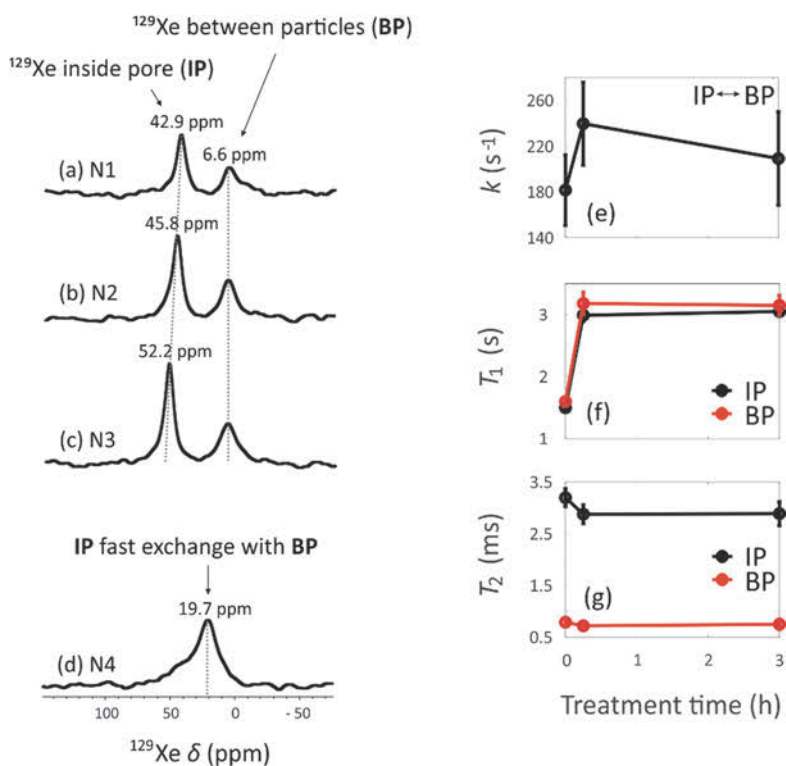
Fig. 29. ^{129}Xe spectra of (a) N1, (b) N2, (c) N3, and (d) N4. ^{129}Xe dynamic: (e) exchange rate (*k*) between sites IP and BP, (f) T_1, and (g) T_2 of two sites as a function of NH_4OH treatment times in 3 h (Adapted, with permission, from Paper IV © 2022 Authors).
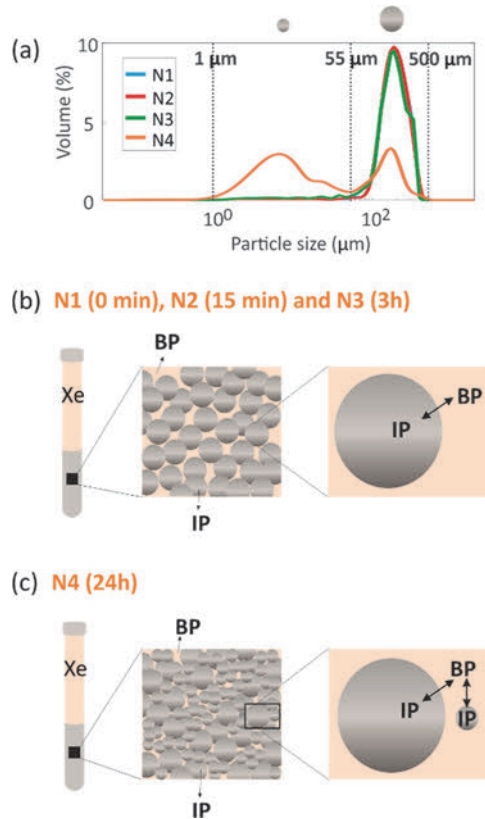
Fig. 30. (a) Particle-size distributions of the four samples measured using a laser diffraction particle-size analyzer. Assumed xenon gas exchange between IP and BP of (b) N1, N2, and N3, and (c) N4 (Adapted, with permission, from Paper IV © 2022 Authors).

4.4.2 Pore sites and pore connectivity

To detect the pore structure inside particles, water was employed as probe liquid, and ^{1}H relaxation NMR methods were used. The 1D ^{1}H T_2 and T_1 distributions were acquired, and 2D ^{1}H T_1–T_2 and T_2–T_2 maps were collected.

T_2–T_2 maps (Figs. 31a, 31c, 31e and 31g) and 1D T_2 distributions sub-plotted on the top of them show four components. The component labeled with BP is water in large voids in-between particles. The peak S represents small pores. Two middle peaks between BP and S are assumed to be one class of big pores, as only one middle peak with 17 ms of T_1 is shown in T_1–T_2 maps (Figs. 31b, 31d, 31f, and 31h). They are labeled as B. Pore B appearing as two separate middle peaks may

result from the over-calculation of the number of components when T_2 data were fitted.

The 1D T_1 distributions (sub-plotted on the right side of T_1–T_2 maps) show two peaks, which are attributed to the water inside pore (IP) and the water between particles (BP). The smaller number of detected pore sites than for T_2 data means that T_1 is more impacted by the exchange process.

The ratio of the signal intensities between S with B (S/B) derived from CPMG experiments are shown in Table 2. The N1 to N3 has an S/B of 2, while S/B decreases to 1 for N4. The following two assumptions can be raised up for this change when the NH_4OH treatment time increases from 3 h to 24 h. One is that the pore connectivity between S with B is enhanced and the faster exchange weights S/B. The components derived from T_2 data has been found to be weighted by exchange process [127]. Another one is that a portion of small pores (S) enlarge into big pores (B).

The change in pore connectivity with increasing NH_4OH treatment time is also reflected from the exchange peaks in T_2–T_2 and T_1–T_2 spectra. The water exchange between pore S and outside pores (BP) is observed for N1, N2, and N3 in T_2–T_2 maps (Figs. 31a, 31c, 31e and 32a). However, after 24 h NH_4OH treatment, the exchange between S and B (Fig. 32b) is shown in both T_2–T_2 (Fig. 31g) and T_1–T_2 spectra (Fig. 31h). Two assumptions can be come up with: One is that N4 has enhanced inner pore connectivity compared to other samples, leading to the obvious S-B exchange peak; another one is that the low signal intensity of B for N1, N2, and N3 may lead to the invisibility of their exchange peak. If the second case is true, it means that N4 has more B pores than the other samples. These two assumptions agree well with the two assumptions raising from the CPMG S/B data.
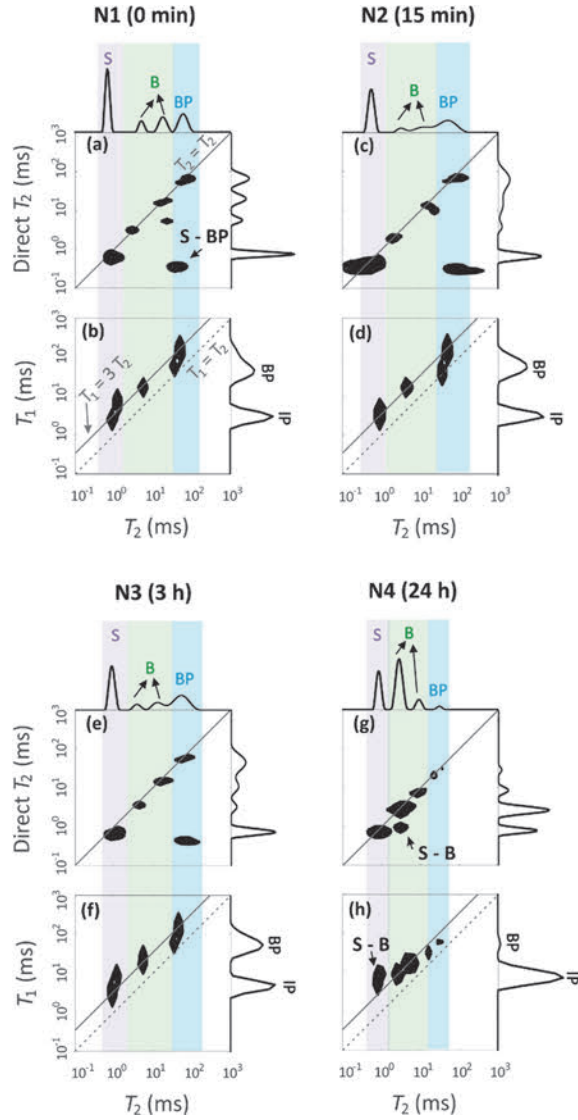
Fig. 31. 2D ¹H relaxation maps of (a, b) N1, (c, d) N2, (e, f) N3, and (g, h) N4 with fully water-saturated: (a, c, e, and g) ¹H T_2–T_2 maps with 0.2-ms mixing time and (b, d, f, and h) ¹H T_1–T_2 maps. On the T_2–T_2 maps, the diagonal lines are $T_2 = T_2$. On the T_1–T_2 maps, the dashed diagonal lines are $T_1 = T_2$ and the solid diagonal lines are $T_1 = 3T_2$. 1D T_2 distributions were sub-plotted on the top of T_2–T_2 maps, and T_1 distributions were sub-plotted on the right side of T_1–T_2 maps (Adapted, with permission, from Paper IV © 2022 Authors).

Table 2. Percentages of signal intensities of S and B from CPMG experiments of four geopolymers with different NH₄OH treatment times, as well as the portion between S with B (Adapted, with permission, from Paper IV © 2022 Authors).

CPMG	S	B	S/B
N1 (0 min)	70%	30%	2.33
N2 (15 min)	71%	29%	2.44
N3 (3 h)	68%	33%	2.06
N4 (24 h)	53%	47%	1.13
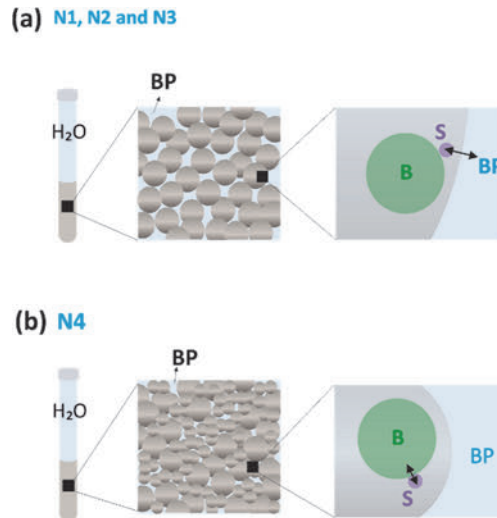
Fig. 32. Assumed water exchange within three sites: S, B, and BP of (a) N1, N2, and N3, and (b) N4 (Adapted, with permission, from Paper IV © 2022 Authors).

4.4.3 Pore size

The pore sizes were measured to provide more information about pore structures. The VT ^{129}Xe spectra were applied to measure the averaged pore size for N1, N2, and N3 samples. The ^{1}H NMR cryoporometry and N$_2$ physisorption were applied to acquire PSDs for all samples.

The VT ^{129}Xe spectra collected from 212 K to 324 K (Fig. 33a) show that the averaged pore sizes of all the pores inside particles were almost the same for N1, N2, and N3, at around 6 nm (Fig. 33c).

The N$_2$ physisorption (Fig. 34b) shows one peak at about 7 nm, while the ^{1}H cryoporometry (Fig. 34a) shows three peaks for all samples. The peak at 100 nm is

free water. The micropore at about 1.7 nm corresponds to the pore S in Fig. 31. This micropore in not visible in the N_2 physisorption PSDs because it is out of the lower limit of BJH analysis. The mesopore at around 7 nm corresponds to the pore size detected by N_2 physisorption.

As shown in Table 3, the percentages of signal intensities between S and B (S/B) of ^{1}H NMR cryoporometry are close to the S/B from CPMG experiments (Table 2) for the samples treated within 3 h, which is about 2. N4 does not change their S/B of cryoporometry signal, whereas the CPMG percentage of N4 changes to 1. This may be because the cryoporometry experiments do not reflect the water dynamics, but T_2 data are affected by enhanced pore connectivity. Combining S/B results acquired from NMR cryoporometry with two assumptions derived from S/B of CPMG (Table 2) and exchange peaks on 2D relaxation maps (Fig. 31), one thing is for sure that after 24 h NH_4OH treatment, the S did not enlarge to B because S/B of cryoporometry signal stays stable. The changed S/B of CPMG signal (Table 2) and exchange peak of N4 (Figs. 31g and 31h) are consequences of the enhanced pore connectivity between S and B.
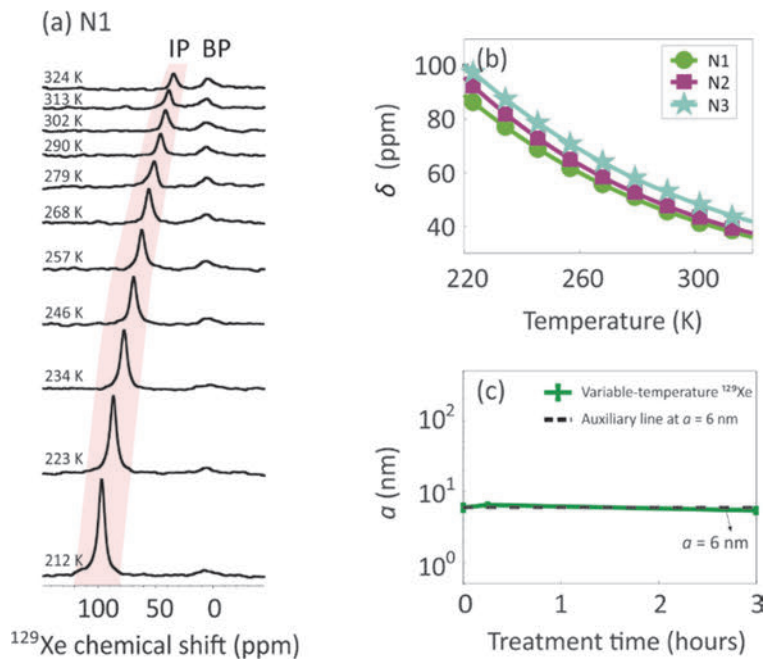
Fig. 33. (a) VT ^{129}Xe spectra of N1, (b) chemical shifts of peak IP as a function of temperature, and (c) averaged pore diameter as a function of NH$_4$OH treatment time (Adapted, with permission, from Paper IV © 2022 Authors).
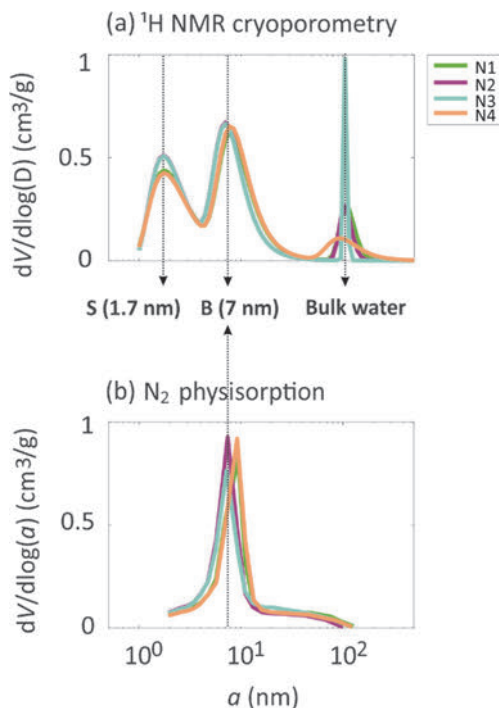
Fig. 34. PSDs acquired from (a) ^{1}H NMR cryoporometry and (b) N$_2$ physisorption (Adapted, with permission, from Paper IV © 2022 Authors).

Table 3. Percentages of signal intensities of S and B from cryoporometry experiments fitted by Eq. 24 of four geopolymers with different NH$_4$OH treatment times (Adapted, with permission, from Paper IV © 2022 Authors).

Cryoporometry	S	B	S/B
N1 (0 min)	63%	37%	2.33
N2 (15 min)	68%	32%	2.13
N3 (3 h)	68%	32%	2.13
N4 (24 h)	68%	32%	2.13

Combining ^{129}Xe with ^{1}H NMR methods, Paper IV shows that NH$_4$OH posttreatment is a good way to enhance pore connectivity without changing the pore size of geopolymer. However, when conducting the NH$_4$OH treatment to zeolites, the pore connectivity is also enhanced, and partial micropores are enlarged to mesopores at the same time [128].

78

5   Summary and conclusions

The porous structure, including pore sites, sizes, and connectivity of geopolymers, was comprehensively studied using advanced NMR methods. The ^{1}H relaxometry and NMR cryoporometry methods were able to detect the pore structures nondestructively using inherent water in the system as a probe fluid. The ^{129}Xe NMR spectra, selective IR, and relaxometry methods detected the pore connectivity more efficiently and comprehensively than other methods. The application of the single-sided NMR device also helped to overcome limitations stemming from the size of the specimen in NMR analysis. Additionally, the effect of three factors, *w/s*, *Si/Al*, and NH$_4$OH posttreatment on the geopolymerization/curing and the pore structures were investigated.

Paper I applied ^{1}H relaxometry and NMR cryoporometry methods to study the pore structures of geopolymer in a nondestructive way. The evolution of pore sizes during curing and cured pore structure were both detected. Three mesopores, zeolite-analog pores, geopolymer disordered pores, and defective pores, were found in geopolymers. The zeolite-analog pores were connected using the geopolymer disordered pores. The geopolymer disordered pores and defective pores were found to become increase with the *w/s*. This finding of varying pore structures with *w/s* can be related to mechanical properties when geopolymers work as construction materials.

Paper II applied ^{129}Xe NMR methods to detect the pore structures of geopolymers in a wider *w/s* range. ^{129}Xe NMR was able to detect pore sites, sizes, and connectivity efficiently. Three pore sites were again found for the samples with *w/s* of 0.66 to 0.50, in agreement with the ^{1}H results in Paper I. However, the sample with *w/s* of 0.75 did not show zeolite-analog pores. ^{129}Xe EXSY, selective IR, and relaxometry showed that all the pores were efficiently interconnected. The increased *w/s* was found to lead to not only larger pore sizes but also enhanced pore connectivity. This finding has two consequences. This method can be applied to study the relationship between pore connectivity and permeability when geopolymers are applied in the building industry. The inborn mesopores and the efficient pore connectivity also provide the basis for using geopolymers as more efficient catalysts than zeolites in some catalysis systems.

Paper III revealed the effect of *Si/Al* on the geopolymerization and pore structure by a single-sided NMR device, NMR-MOUSE. This device is free from the limitation of the small size of the specimen for traditional NMR experiments. When the low *Si/Al* of 1 was used, five stages and two gel phases were found: one

gel with an *Si/Al* of 1 and another gel with an *Si/Al* of 2. Three stages and one gel phase (with an *Si/Al* of 2) were found for the samples with an *Si/Al* of 1.5, 2, and 2.5. The presence of two gel phases during geopolymerization was assumed to be the main reason for the growth of zeolite-analog pores. This work provided a way to trace the pore structures of geopolymers back to their growth process.

Paper IV investigated the effect of NH_4OH posttreatment on the pore structure by combining ^1H and ^{129}Xe NMR methods. Micropores (1.7 nm) and mesopores (about 7 nm) were found to be accessible both with and without the NH_4OH treatment. Their pore sizes did not change as the NH_4OH posttreatment time increased, but the pore connectivity between two pores was enhanced after a 24 h NH_4OH treatment. This provided a mild way to tailor the pore structure of geopolymer, which gave well-preserved pore size but enhanced pore connectivity of the whole pore system. This approach makes geopolymers more attractive as catalysts in catalysis processes.

In conclusion, the ^1H and ^{129}Xe NMR analysis gave a full understanding of geopolymerization processes and geopolymers' pore structures. Geopolymers were found to develop from the geopolymerization process, comprising dissolution, various gelation, and condensation stages. A micropore and several mesopores were found to be inborn and connected in cured geopolymers, providing the basis for the development of geopolymers for catalysis applications. Additionally, the *w/s*, *Si/Al,* and NH_4OH posttreatment were found to be the three effective methods in the tailoring of the pore structures of geopolymers, also allowing for modification of mechanical properties.

List of references

[1] B. Majidi, "Geopolymer technology, from fundamentals to advanced applications: a review," *Materials Technology*, vol. 24, no. 2, pp. 79–87, Jun. 2009, doi: 10.1179/175355509X449355.

[2] B. Singh, G. Ishwarya, M. Gupta, and S. K. Bhattacharyya, "Geopolymer concrete: A review of some recent developments," *Construction and Building Materials*, vol. 85, pp. 78–90, Jun. 2015, doi: 10.1016/j.conbuildmat.2015.03.036.

[3] G. Habert, J. B. d'Espinose de Lacaillerie, and N. Roussel, "An environmental evaluation of geopolymer based concrete production: reviewing current research trends," *Journal of Cleaner Production*, vol. 19, no. 11, pp. 1229–1238, Jul. 2011, doi: 10.1016/j.jclepro.2011.03.012.

[4] C.-K. Ma, A. Z. Awang, and W. Omar, "Structural and material performance of geopolymer concrete: A review," *Construction and Building Materials*, vol. 186, pp. 90–102, Oct. 2018, doi: 10.1016/j.conbuildmat.2018.07.111.

[5] P. Sazama, O. Bortnovsky, J. Dědeček, Z. Tvarůžková, and Z. Sobalík, "Geopolymer based catalysts—New group of catalytic materials," *Catalysis Today*, vol. 164, no. 1, pp. 92–99, Apr. 2011, doi: 10.1016/j.cattod.2010.09.008.

[6] N. Ariffin, M. M. A. B. Abdullah, R. R. M. A. Zainol, and M. F. Murshed, "Geopolymer as an adsorbent of heavy metal: A review," *AIP Conference Proceedings*, vol. 1885, no. 1, p. 020030, Sep. 2017, doi: 10.1063/1.5002224.

[7] L. Biondi, M. Perry, J. McAlorum, C. Vlachakis, and A. Hamilton, "Geopolymer-based moisture sensors for reinforced concrete health monitoring," *Sensors and Actuators B: Chemical*, vol. 309, p. 127775, Apr. 2020, doi: 10.1016/j.snb.2020.127775.

[8] N. A. Jaya, L. Yun-Ming, H. Cheng-Yong, M. M. A. B. Abdullah, and K. Hussin, "Correlation between pore structure, compressive strength and thermal conductivity of porous metakaolin geopolymer," *Construction and Building Materials*, vol. 247, p. 118641, Jun. 2020, doi: 10.1016/j.conbuildmat.2020.118641.

[9] A. G. Slater and A. I. Cooper, "Function-led design of new porous materials," *Science*, vol. 348, no. 6238, p. aaa8075, May 2015, doi: 10.1126/science.aaa8075.

[10] B. E. Glad and W. M. Kriven, "Optimization of Gas Adsorption Porosimetry for Geopolymer Analysis," *Journal of the American Ceramic Society*, vol. 96, no. 11, pp. 3643–3649, 2013, doi: 10.1111/jace.12578.

[11] F. G. M. Aredes, T. M. B. Campos, J. P. B. Machado, K. K. Sakane, G. P. Thim, and D. D. Brunelli, "Effect of cure temperature on the formation of metakaolinite-based geopolymer," *Ceramics International*, vol. 41, no. 6, pp. 7302–7311, Jul. 2015, doi: 10.1016/j.ceramint.2015.02.022.

[12] P. Duxson, J. L. Provis, G. C. Lukey, S. W. Mallicoat, W. M. Kriven, and J. S. J. van Deventer, "Understanding the relationship between geopolymer composition, microstructure and mechanical properties," *Colloids and Surfaces A: Physicochemical and Engineering Aspects*, vol. 269, no. 1, pp. 47–58, Nov. 2005, doi: 10.1016/j.colsurfa.2005.06.060.

[13] J. L. Provis, R. J. Myers, C. E. White, V. Rose, and J. S. J. van Deventer, "X-ray microtomography shows pore structure and tortuosity in alkali-activated binders," *Cement and Concrete Research*, vol. 42, no. 6, pp. 855–864, Jun. 2012, doi: 10.1016/j.cemconres.2012.03.004.

[14] S. Lee, H.-T. Jou, A. van Riessen, W. D. A. Rickard, C.-M. Chon, and N.-H. Kang, "Three-dimensional quantification of pore structure in coal ash-based geopolymer using conventional electron tomography," *Construction and Building Materials*, vol. 52, pp. 221–226, Feb. 2014, doi: 10.1016/j.conbuildmat.2013.10.072.

[15] P. F. Faure and S. Rodts, "Proton NMR relaxation as a probe for setting cement pastes," *Magnetic Resonance Imaging*, vol. 26, no. 8, pp. 1183–1196, Oct. 2008, doi: 10.1016/j.mri.2008.01.026.

[16] P. J. McDonald, J.-P. Korb, J. Mitchell, and L. Monteilhet, "Surface relaxation and chemical exchange in hydrating cement pastes: A two-dimensional NMR relaxation study," *Phys. Rev. E*, vol. 72, no. 1, p. 011409, Jul. 2005, doi: 10.1103/PhysRevE.72.011409.

[17] R. M. E. Valckenborg, L. Pel, and K. Kopinga, "Combined NMR cryoporometry and relaxometry," *J. Phys. D: Appl. Phys.*, vol. 35, no. 3, pp. 249–256, Jan. 2002, doi: 10.1088/0022-3727/35/3/314.

[18] J.-L. Bonardet, J. Fraissard, A. Gédéon, and M.-A. Springuel-Huet, "Nuclear Magnetic Resonance of Physisorbed 129Xe Used as a Probe to Investigate Porous Solids," *Catalysis Reviews*, vol. 41, no. 2, pp. 115–225, May 1999, doi: 10.1080/01614949909353779.

[19] J. Davidovits, *Soft Mineralurgy and Geopolymers*, vol. 1. 1988, p. 23.

[20] N. B. Singh, S. K. Saxena, M. Kumar, and S. Rai, "Geopolymer cement: Synthesis, Characterization, Properties and applications," *Materials Today: Proceedings*, vol. 15, pp. 364–370, Jan. 2019, doi: 10.1016/j.matpr.2019.04.095.

[21] P. Duxson, "The structure and thermal evolution of metakaolin geopolymers," Ph.D. dissertation, Dept. Chemical & Biomolecular Engineering, Univ. Melbourne., Melbourne, Australia, Feb. 2006, Accessed: Apr. 03, 2022. [Online]. Available: http://hdl.handle.net/11343/39114

[22] "Concrete needs to lose its colossal carbon footprint," *Nature*, vol. 597, no. 7878, pp. 593–594, Sep. 2021, doi: 10.1038/d41586-021-02612-5.

[23] E. Benhelal, G. Zahedi, and H. Hashim, "A novel design for green and economical cement manufacturing," *Journal of Cleaner Production*, vol. 22, no. 1, pp. 60–66, Feb. 2012, doi: 10.1016/j.jclepro.2011.09.019.

[24] K. Neupane, D. Chalmers, and P. Kidd, "High-Strength Geopolymer Concrete-Properties, Advantages and Challenges," *Advances in Materials*, vol. 7, Jun. 2018, doi: 10.11648/j.am.20180702.11.

[25] M. Lahoti, K. H. Tan, and E.-H. Yang, "A critical review of geopolymer properties for structural fire-resistance applications," *Construction and Building Materials*, vol. 221, pp. 514–526, Oct. 2019, doi: 10.1016/j.conbuildmat.2019.06.076.

[26] B. Singh, G. Ishwarya, M. Gupta, and S. K. Bhattacharyya, "Geopolymer concrete: A review of some recent developments," *Construction and Building Materials*, vol. 85, pp. 78–90, Jun. 2015, doi: 10.1016/j.conbuildmat.2015.03.036.

[27] J. S. J. van Deventer, C. E. White, and R. J. Myers, "A Roadmap for Production of Cement and Concrete with Low-CO2 Emissions," *Waste Biomass Valor*, vol. 12, no. 9, pp. 4745–4775, Sep. 2021, doi: 10.1007/s12649-020-01180-5.

[28] T. Glasby, J. Day, R. Genrich, and D. J. Aldred, "EFC Geopolymer Concrete Aircraft Pavements at Brisbane West Wellcamp Airport," presented at the Concrete 2015 Conference, Melbourne, Australia, pp. 1–9, 2015.

[29] P. Sazama, O. Bortnovsky, J. Dědeček, Z. Tvarůžková, and Z. Sobalík, "Geopolymer based catalysts—New group of catalytic materials," *Catalysis Today*, vol. 164, no. 1, pp. 92–99, Apr. 2011, doi: 10.1016/j.cattod.2010.09.008.

[30] G. A. Ozin, A. Kuperman, and A. Stein, "Advanced Zeolite, Materials Science," *Angewandte Chemie International Edition in English*, vol. 28, no. 3, pp. 359–376, 1989, doi: 10.1002/anie.198903591.

[31] A. Noushini and A. Castel, "The effect of heat-curing on transport properties of low-calcium fly ash-based geopolymer concrete," *Construction and Building Materials*, vol. 112, pp. 464–477, Jun. 2016, doi: 10.1016/j.conbuildmat.2016.02.210.

[32] J. R. Holst and A. I. Cooper, "Ultrahigh Surface Area in Porous Solids," *Advanced Materials*, vol. 22, no. 45, pp. 5212–5216, 2010, doi: 10.1002/adma.201002440.

[33] Y. Zhang, W. Zhang, W. Sun, Z. Li, and Z. Liu, "Preparation of metakaolin based geopolymer and its three-dimensional pore structural characterization," *J. Wuhan Univ. Technol.-Mat. Sci. Edit.*, vol. 30, no. 3, pp. 550–555, Jun. 2015, doi: 10.1007/s11595-015-1187-5.

[34] P. Duxson, A. Fernández-Jiménez, J. L. Provis, G. C. Lukey, A. Palomo, and J. S. J. van Deventer, "Geopolymer technology: the current state of the art," *J Mater Sci*, vol. 42, no. 9, pp. 2917–2933, May 2007, doi: 10.1007/s10853-006-0637-z.

[35] A. Fernández-Jiménez, A. Palomo, I. Sobrados, and J. Sanz, "The role played by the reactive alumina content in the alkaline activation of fly ashes," *Microporous and Mesoporous Materials*, vol. 91, no. 1, pp. 111–119, Apr. 2006, doi: 10.1016/j.micromeso.2005.11.015.

[36] A. Hajimohammadi, J. L. Provis, and J. S. J. van Deventer, "Effect of Alumina Release Rate on the Mechanism of Geopolymer Gel Formation," *Chem. Mater.*, vol. 22, no. 18, pp. 5199–5208, Sep. 2010, doi: 10.1021/cm101151n.

[37] C. E. White, J. L. Provis, A. Llobet, T. Proffen, and J. S. J. van Deventer, "Evolution of Local Structure in Geopolymer Gels: An In Situ Neutron Pair Distribution Function Analysis," *Journal of the American Ceramic Society*, vol. 94, no. 10, pp. 3532–3539, 2011, doi: 10.1111/j.1551-2916.2011.04515.x.

[38] A. Fernández-Jiménez, A. Palomo, and M. Criado, "Microstructure development of alkali-activated fly ash cement: a descriptive model," *Cement and Concrete Research*, vol. 35, no. 6, pp. 1204–1209, Jun. 2005, doi: 10.1016/j.cemconres.2004.08.021.

[39] J. L. Provis, P. Duxson, J. S. J. Van Deventer, and G. C. Lukey, "The Role of Mathematical Modelling and Gel Chemistry in Advancing Geopolymer Technology," *Chemical Engineering Research and Design*, vol. 83, no. 7, pp. 853–860, Jul. 2005, doi: 10.1205/cherd.04329.

[40] V.D. Glukhovsky, "Soil Silicates," *Gosstroyizdat USSR*, Kiev, 1959.

[41] X. Yao, Z. Zhang, H. Zhu, and Y. Chen, "Geopolymerization process of alkali–metakaolinite characterized by isothermal calorimetry," *Thermochimica Acta*, vol. 493, no. 1, pp. 49–54, Sep. 2009, doi: 10.1016/j.tca.2009.04.002.

[42] L. Weng and K. Sagoe-Crentsil, "Dissolution processes, hydrolysis and condensation reactions during geopolymer synthesis: Part I—Low Si/Al ratio systems," *J Mater Sci*, vol. 42, no. 9, pp. 2997–3006, May 2007, doi: 10.1007/s10853-006-0820-2.

[43] K. Sagoe-Crentsil and L. Weng, "Dissolution processes, hydrolysis and condensation reactions during geopolymer synthesis: Part II. High Si/Al ratio systems," *J Mater Sci*, vol. 42, no. 9, pp. 3007–3014, May 2007, doi: 10.1007/s10853-006-0818-9.

[44] J. S. J. van Deventer, J. L. Provis, P. Duxson, and G. C. Lukey, "Reaction mechanisms in the geopolymeric conversion of inorganic waste to useful products," *Journal of Hazardous Materials*, vol. 139, no. 3, pp. 506–513, Jan. 2007, doi: 10.1016/j.jhazmat.2006.02.044.

[45] Z. Hu, M. Wyrzykowski, and P. Lura, "Estimation of reaction kinetics of geopolymers at early ages," *Cement and Concrete Research*, vol. 129, p. 105971, Mar. 2020, doi: 10.1016/j.cemconres.2020.105971.

[46] J. L. Provis and J. S. J. van Deventer, "Geopolymerisation kinetics. 1. In situ energy-dispersive X-ray diffractometry," *Chemical Engineering Science*, vol. 62, no. 9, pp. 2309–2317, May 2007, doi: 10.1016/j.ces.2007.01.027.

[47] J. L. Provis and J. S. J. van Deventer, "Geopolymerisation kinetics. 2. Reaction kinetic modelling," *Chemical Engineering Science*, vol. 62, no. 9, pp. 2318–2329, May 2007, doi: 10.1016/j.ces.2007.01.028.

[48] A. A. Siyal, K. A. Azizli, Z. Man, L. Ismail, and M. I. Khan, "Geopolymerization kinetics of fly ash based geopolymers using JMAK model," *Ceramics International*, vol. 42, no. 14, pp. 15575–15584, Nov. 2016, doi: 10.1016/j.ceramint.2016.07.006.

[49] H. Rahier, J. Wastiels, M. Biesemans, R. Willlem, G. Van Assche, and B. Van Mele, "Reaction mechanism, kinetics and high temperature transformations of geopolymers," *J Mater Sci*, vol. 42, no. 9, pp. 2982–2996, May 2007, doi: 10.1007/s10853-006-0568-8.

[50] C. Shi, A. F. Jiménez, and A. Palomo, "New cements for the 21st century: The pursuit of an alternative to Portland cement," *Cement and Concrete Research*, vol. 41, no. 7, pp. 750–763, Jul. 2011, doi: 10.1016/j.cemconres.2011.03.016.

[51] W. K. Part, M. Ramli, and C. B. Cheah, "An overview on the influence of various factors on the properties of geopolymer concrete derived from industrial by-products," *Construction and Building Materials*, vol. 77, pp. 370–395, Feb. 2015, doi: 10.1016/j.conbuildmat.2014.12.065.

[52] D. Khale and R. Chaudhary, "Mechanism of geopolymerization and factors influencing its development: a review," *J Mater Sci*, vol. 42, no. 3, pp. 729–746, Feb. 2007, doi: 10.1007/s10853-006-0401-4.

[53] K. Chen, D. Wu, L. Xia, Q. Cai, and Z. Zhang, "Geopolymer concrete durability subjected to aggressive environments – A review of influence factors and comparison with ordinary Portland cement," *Construction and Building Materials*, vol. 279, p. 122496, Apr. 2021, doi: 10.1016/j.conbuildmat.2021.122496.

[54] A. Hassan, M. Arif, and M. Shariq, "Use of geopolymer concrete for a cleaner and sustainable environment – A review of mechanical properties and microstructure," *Journal of Cleaner Production*, vol. 223, pp. 704–728, Jun. 2019, doi: 10.1016/j.jclepro.2019.03.051.

[55] M. Clausi, S. C. Tarantino, L. L. Magnani, M. P. Riccardi, C. Tedeschi, and M. Zema, "Metakaolin as a precursor of materials for applications in Cultural Heritage: Geopolymer-based mortars with ornamental stone aggregates," *Applied Clay Science*, vol. 132–133, pp. 589–599, Nov. 2016, doi: 10.1016/j.clay.2016.08.009.

[56] Z. Zuhua, Y. Xiao, Z. Huajun, and C. Yue, "Role of water in the synthesis of calcined kaolin-based geopolymer," *Applied Clay Science*, vol. 43, no. 2, pp. 218–223, Feb. 2009, doi: 10.1016/j.clay.2008.09.003.

[57] S. Mu *et al.*, "Property and microstructure of aluminosilicate inorganic coating for concrete: Role of water to solid ratio," *Construction and Building Materials*, vol. 148, pp. 846–856, Sep. 2017, doi: 10.1016/j.conbuildmat.2017.05.070.

[58] Q. Wan, Y. Zhang, and R. Zhang, "The effect of pore behavior and gel structure on the mechanical property at different initial water content," *Construction and Building Materials*, vol. 309, p. 125146, Nov. 2021, doi: 10.1016/j.conbuildmat.2021.125146.

[59] N. Ye *et al.*, "Synthesis and strength optimization of one-part geopolymer based on red mud," *Construction and Building Materials*, vol. 111, pp. 317–325, May 2016, doi: 10.1016/j.conbuildmat.2016.02.099.

[60] A. Dehghani, F. Aslani, and N. Ghaebi Panah, "Effects of initial SiO2/Al2O3 molar ratio and slag on fly ash-based ambient cured geopolymer properties," *Construction and Building Materials*, vol. 293, p. 123527, Jul. 2021, doi: 10.1016/j.conbuildmat.2021.123527.

[61] K. Juengsuwattananon, F. Winnefeld, P. Chindaprasirt, and K. Pimraksa, "Correlation between initial SiO2/Al2O3, Na2O/Al2O3, Na2O/SiO2 and H2O/Na2O ratios on phase and microstructure of reaction products of metakaolin-rice husk ash geopolymer," *Construction and Building Materials*, vol. 226, pp. 406–417, Nov. 2019, doi: 10.1016/j.conbuildmat.2019.07.146.

[62] M. Lahoti, K. K. Wong, E.-H. Yang, and K. H. Tan, "Effects of Si/Al molar ratio on strength endurance and volume stability of metakaolin geopolymers subject to elevated temperature," *Ceramics International*, vol. 44, no. 5, pp. 5726–5734, Apr. 2018, doi: 10.1016/j.ceramint.2017.12.226.

85

[63]   S. Mu, J. Liu, J. Liu, Y. Wang, L. Shi, and Q. Jiang, "Property and Microstructure of Waterborne Self-Setting Geopolymer Coating: Optimization Effect of SiO2/Na2O Molar Ratio," *Minerals*, vol. 8, no. 4, Art. no. 4, Apr. 2018, doi: 10.3390/min8040162.

[64]   Y.-K. Cho, S.-W. Yoo, S.-H. Jung, K.-M. Lee, and S.-J. Kwon, "Effect of Na2O content, SiO2/Na2O molar ratio, and curing conditions on the compressive strength of FA-based geopolymer," *Construction and Building Materials*, vol. 145, pp. 253–260, Aug. 2017, doi: 10.1016/j.conbuildmat.2017.04.004.

[65]   K. Gao *et al.*, "Effects SiO2/Na2O molar ratio on mechanical properties and the microstructure of nano-SiO2 metakaolin-based geopolymers," *Construction and Building Materials*, vol. 53, pp. 503–510, Feb. 2014, doi: 10.1016/j.conbuildmat.2013.12.003.

[66]   J. V. Aelst *et al.*, "Catalyst Design by NH4OH Treatment of USY Zeolite," *Advanced Functional Materials*, vol. 25, no. 46, pp. 7130–7144, 2015, doi: https://doi.org/10.1002/adfm.201502772.

[67]   J. Van Aelst *et al.*, "Hierarchization of USY Zeolite by NH4OH. A Postsynthetic Process Investigated by NMR and XRD," *J. Phys. Chem. C*, vol. 118, no. 39, pp. 22573–22582, Oct. 2014, doi: 10.1021/jp5058594.

[68]   J. Keeler, *Understanding NMR spectroscopy*, 2nd ed. New York, USA: John Wiley & Sons, 2011.

[69]   J. B. Lambert, E. P. Mazzola, and C. D. Ridge, *Nuclear Magnetic Resonance Spectroscopy: An Introduction to Principles, Applications, and Experimental Methods*. New York, USA: John Wiley & Sons, 2019.

[70]   B. P. Cowan, *Nuclear magnetic resonance and relaxation*. New York, USA: Cambridge University Press, 1997.

[71]   W. R. Croasmun and R. M. K. Carlson, *Two-Dimensional NMR Spectroscopy: Applications for Chemists and Biochemists*. New York, USA: John Wiley & Sons, 1996.

[72]   A. J. Vega and G. W. Scherer, "Study of structural evolution of silica gel using 1H and 29Si NMR," *Journal of Non-Crystalline Solids*, vol. 111, no. 2, pp. 153–166, Nov. 1989, doi: 10.1016/0022-3093(89)90276-7.

[73]   R. M. E. Valckenborg, L. Pel, and K. Kopinga, "Combined NMR cryoporometry and relaxometry," *J. Phys. D: Appl. Phys.*, vol. 35, no. 3, pp. 249–256, Jan. 2002, doi: 10.1088/0022-3727/35/3/314.

[74]   P. J. McDonald, J.-P. Korb, J. Mitchell, and L. Monteilhet, "Surface relaxation and chemical exchange in hydrating cement pastes: A two-dimensional NMR relaxation study," *Phys. Rev. E*, vol. 72, no. 1, p. 011409, Jul. 2005, doi: 10.1103/PhysRevE.72.011409.

[75]   P. Rejmak, J. S. Dolado, M. J. Stott, and A. Ayuela, "29Si NMR in Cement: A Theoretical Study on Calcium Silicate Hydrates," *J. Phys. Chem. C*, vol. 116, no. 17, pp. 9755–9761, May 2012, doi: 10.1021/jp302218j.

[76] E. Lippmaa, M. Maegi, A. Samoson, M. Tarmak, and G. Engelhardt, "Investigation of the structure of zeolites by solid-state high-resolution silicon-29 NMR spectroscopy," *J. Am. Chem. Soc.*, vol. 103, no. 17, pp. 4992–4996, Aug. 1981, doi: 10.1021/ja00407a002.

[77] J. Kärger and H. Pfeifer, "N.m.r. self-diffusion studies in zeolite science and technology," *Zeolites*, vol. 7, no. 2, pp. 90–107, Mar. 1987, doi: 10.1016/0144-2449(87)90067-4.

[78] C. Dybowski, N. Bansal, and T. M. Duncan, "NMR Spectroscopy of Xenon in Confined Spaces: Clathrates, Intercalates, and Zeolites," *Annual Review of Physical Chemistry*, vol. 42, no. 1, pp. 433–464, 1991, doi: 10.1146/annurev.pc.42.100191.002245.

[79] G. Liu, Y. Li, and J. Jonas, "Confined geometry effects on reorientational dynamics of molecular liquids in porous silica glasses," *J. Chem. Phys.*, vol. 95, no. 9, pp. 6892–6901, Nov. 1991, doi: 10.1063/1.461501.

[80] F. Stallmach *et al.*, "NMR Studies on the Diffusion of Hydrocarbons on the Metal-Organic Framework Material MOF-5," *Angewandte Chemie International Edition*, vol. 45, no. 13, pp. 2123–2126, 2006, doi: 10.1002/anie.200502553.

[81] S. Devautour-Vinot *et al.*, "Structure and Dynamics of the Functionalized MOF Type UiO-66(Zr): NMR and Dielectric Relaxation Spectroscopies Coupled with DFT Calculations," *Chem. Mater.*, vol. 24, no. 11, pp. 2168–2177, Jun. 2012, doi: 10.1021/cm300863c.

[82] X.-P. Tang *et al.*, "Electronic Structures of Single-Walled Carbon Nanotubes Determined by NMR," *Science*, Apr. 2000, doi: 10.1126/science.288.5465.492.

[83] C. Goze-Bac *et al.*, "Magnetic interactions in carbon nanostructures," *Carbon*, vol. 40, no. 10, pp. 1825–1842, Aug. 2002, doi: 10.1016/S0008-6223(02)00061-1.

[84] M. Pons, *NMR in Supramolecular Chemistry*. Springer Science & Business Media, 2012.

[85] E. L. Hahn, "Nuclear Induction Due to Free Larmor Precession," *Phys. Rev.*, vol. 77, no. 2, pp. 297–298, Jan. 1950, doi: 10.1103/PhysRev.77.297.2.

[86] K. Jozef and M. Lena, *Nuclear Spin Relaxation in Liquids: Theory, Experiments, and Applications*, 2nd ed. Boca Raton, USA: CRC Press, 2017.

[87] H. W. Spiess, "Rotation of Molecules and Nuclear Spin Relaxation," in *Dynamic NMR Spectroscopy*, Berlin, Heidelberg, 1978, pp. 55–214. doi: 10.1007/978-3-642-66961-3_2.

[88] R. L. Vold, J. S. Waugh, M. P. Klein, and D. E. Phelps, "Measurement of Spin Relaxation in Complex Systems," *The Journal of Chemical Physics*, vol. 48, no. 8, pp. 3831–3832, Apr. 1968, doi: 10.1063/1.1669699.

[89] C. F. Davis, M. W. P. Strandberg, and R. L. Kyhl, "Direct Measurement of Electron Spin-Lattice Relaxation Times," *Phys. Rev.*, vol. 111, no. 5, pp. 1268–1272, Sep. 1958, doi: 10.1103/PhysRev.111.1268.

[90] S. Meiboom and D. Gill, "Modified Spin-Echo Method for Measuring Nuclear Relaxation Times," *Review of Scientific Instruments*, vol. 29, no. 8, pp. 688–691, Aug. 1958, doi: 10.1063/1.1716296.

[91]   Y.-Q. Song, "Magnetic Resonance of Porous Media (MRPM): A perspective," *Journal of Magnetic Resonance*, vol. 229, pp. 12–24, Apr. 2013, doi: 10.1016/j.jmr.2012.11.010.

[92]   K. R. Brownstein and C. E. Tarr, "Spin-lattice relaxation in a system governed by diffusion," *Journal of Magnetic Resonance (1969)*, vol. 26, no. 1, pp. 17–24, Apr. 1977, doi: 10.1016/0022-2364(77)90230-X.

[93]   J. Mitchell, L. M. Broche, T. C. Chandrasekera, D. J. Lurie, and L. F. Gladden, "Exploring Surface Interactions in Catalysts Using Low-Field Nuclear Magnetic Resonance," *J. Phys. Chem. C*, vol. 117, no. 34, pp. 17699–17706, Aug. 2013, doi: 10.1021/jp405987m.

[94]   S. Godefroy, J.-P. Korb, M. Fleury, and R. G. Bryant, "Surface nuclear magnetic relaxation and dynamics of water and oil in macroporous media," *Phys. Rev. E*, vol. 64, no. 2, p. 021605, Jul. 2001, doi: 10.1103/PhysRevE.64.021605.

[95]   D. Weber, J. Mitchell, J. McGregor, and L. F. Gladden, "Comparing Strengths of Surface Interactions for Reactants and Solvents in Porous Catalysts Using Two-Dimensional NMR Relaxation Correlations," *J. Phys. Chem. C*, vol. 113, no. 16, pp. 6610–6615, Apr. 2009, doi: 10.1021/jp811246j.

[96]   H. Peemoeller, R. K. Shenoy, and M. M. Pintar, "Two-dimensional nmr time evolution correlation spectroscopy in wet lysozyme," *Journal of Magnetic Resonance (1969)*, vol. 45, no. 2, pp. 193–204, Nov. 1981, doi: 10.1016/0022-2364(81)90116-5.

[97]   S. Vashaee et al., "Local T1-T2 distribution measurements in porous media," *Journal of Magnetic Resonance*, vol. 287, pp. 113–122, Feb. 2018, doi: 10.1016/j.jmr.2018.01.001.

[98]   J. H. Lee, C. Labadie, C. S. Springer, and G. S. Harbison, "Two-dimensional inverse Laplace transform NMR: altered relaxation times allow detection of exchange correlation," *J. Am. Chem. Soc.*, vol. 115, no. 17, pp. 7761–7764, Aug. 1993, doi: 10.1021/ja00070a022.

[99]   L. Venkataramanan, Y.-Q. Song, and M. D. Hurlimann, "Solving Fredholm integrals of the first kind with tensor product structure in 2 and 2.5 dimensions," *IEEE Transactions on Signal Processing*, vol. 50, no. 5, pp. 1017–1026, May 2002, doi: 10.1109/78.995059.

[100] Y.-Q. Song, L. Venkataramanan, M. D. Hürlimann, M. Flaum, P. Frulla, and C. Straley, "T1–T2 Correlation Spectra Obtained Using a Fast Two-Dimensional Laplace Inversion," *Journal of Magnetic Resonance*, vol. 154, no. 2, pp. 261–268, Feb. 2002, doi: 10.1006/jmre.2001.2474.

[101] J. W. Gibbs, *The collected works of J. Willard Gibbs.* New Haven: Yale Univ. Press, 1948. Accessed: Jan. 05, 2022. [Online]. Available: https://catalog.hathitrust.org/Record/004514474

[102] W. Thomson, "LX. On the equilibrium of vapour at a curved surface of liquid," *The London, Edinburgh, and Dublin Philosophical Magazine and Journal of Science*, vol. 42, no. 282, pp. 448–452, Dec. 1871, doi: 10.1080/14786447108640606.

88

[103]   J. H. Strange, M. Rahman, and E. G. Smith, "Characterization of porous solids by NMR," *Phys. Rev. Lett.*, vol. 71, no. 21, pp. 3589–3591, Nov. 1993, doi: 10.1103/PhysRevLett.71.3589.

[104]   J. B. W. Webber, J. C. Dore, J. H. Strange, R. Anderson, and B. Tohidi, "Plastic ice in confined geometry: the evidence from neutron diffraction and NMR relaxation," *J. Phys.: Condens. Matter*, vol. 19, no. 41, p. 415117, Sep. 2007, doi: 10.1088/0953-8984/19/41/415117.

[105]   R. M. E. Valckenborg, L. Pel, and K. Kopinga, "Combined NMR cryoporometry and relaxometry," *J. Phys. D: Appl. Phys.*, vol. 35, no. 3, pp. 249–256, Feb. 2002, doi: 10.1088/0022-3727/35/3/314.

[106]   D. W. Aksnes, K. Førland, and L. Kimtys, "Pore size distribution in mesoporous materials as studied by 1H NMR," *Phys. Chem. Chem. Phys.*, vol. 3, no. 15, pp. 3203–3207, 2001, doi: 10.1039/b103228n.

[107]   E. Weiland, M.-A. Springuel-Huet, A. Nossov, and A. Gédéon, "129Xenon NMR: Review of recent insights into porous materials," *Microporous and Mesoporous Materials*, vol. 225, pp. 41–65, May 2016, doi: 10.1016/j.micromeso.2015.11.025.

[108]   V. V. Terskikh, I. L. Mudrakovskii, and V. M. Mastikhin, "129 Xe nuclear magnetic resonance studies of the porous structure of silica gels," *J. Chem. Soc., Faraday Trans.*, vol. 89, no. 23, pp. 4239–4243, Jan. 1993, doi: 10.1039/FT9938904239.

[109]   J. Jeener, B. H. Meier, P. Bachmann, and R. R. Ernst, "Investigation of exchange processes by two-dimensional NMR spectroscopy," *J. Chem. Phys.*, vol. 71, no. 11, pp. 4546–4553, Dec. 1979, doi: 10.1063/1.438208.

[110]   A. Abragam, "The principles of nuclear magnetism (Clarendon, Oxford)," Goldman M (1984) *Journal of Magnetic Resonance*, vol. 60, pp. 437–452, 1961.

[111]   A. D. Bain and J. A. Cramer, "A Method for Optimizing the Study of Slow Chemical Exchange by NMR Spin-Relaxation Measurements. Application to Tripodal Carbonyl Rotation in a Metal Complex," *Journal of Magnetic Resonance*, vol. 103, pp. 217–222, Jan. 1993, doi: 10.1006/jmra.1993.1156.

[112]   A. D. Bain and J. A. Cramer, "Slow Chemical Exchange in an Eight-Coordinated Bicentered Ruthenium Complex Studied by One-Dimensional Methods. Data Fitting and Error Analysis," *Journal of Magnetic Resonance, Series A*, vol. 118, no. 1, pp. 21–27, Jan. 1996, doi: 10.1006/jmra.1996.0004.

[113]   F. Casanova, J. Perlo, and B. Blümich, "Single-Sided NMR," in *Single-Sided NMR*, F. Casanova, J. Perlo, and B. Blümich, Eds. Berlin, Heidelberg: Springer, 2011, pp. 1–10. doi: 10.1007/978-3-642-16307-4_1.

[114]   H. Y. Carr and E. M. Purcell, "Effects of Diffusion on Free Precession in Nuclear Magnetic Resonance Experiments," *Phys. Rev.*, vol. 94, no. 3, pp. 630–638, May 1954, doi: 10.1103/PhysRev.94.630.

[115]   C. Lamason, B. Macmillan, B. Balcom, B. Leblon, and Z. Pirouz, "Water content measurement in black spruce and aspen sapwood with benchtop and portable magnetic resonance devices," *Wood Material Science & Engineering*, vol. 10, no. 1, pp. 86–93, Jan. 2015, doi: 10.1080/17480272.2015.1010573.

[116] F. de J. C. Barrita, T. W. Bremner, and B. J. Balcom, "Effects of curing temperature on moisture distribution, drying and water absorption in self-compacting concrete," *Magazine of Concrete Research*, May 2015, doi: 10.1680/macr.2003.55.6.517.

[117] L. J. Schreiner *et al.*, "NMR Line Shape-Spin-Lattice Relaxation Correlation Study of Portland Cement Hydration," *Journal of the American Ceramic Society*, vol. 68, no. 1, pp. 10–16, 1985, doi: 10.1111/j.1151-2916.1985.tb15243.x.

[118] J. Ellis and W. Korth, "Removal of geosmin and methylisoborneol from drinking water by adsorption on ultrastable zeolite-Y," *Water Research*, vol. 27, no. 4, pp. 535–539, Apr. 1993, doi: 10.1016/0043-1354(93)90162-B.

[119] V. V. Terskikh *et al.*, "A General Correlation for the 129Xe NMR Chemical Shift−Pore Size Relationship in Porous Silica-Based Materials," *Langmuir*, vol. 18, no. 15, pp. 5653–5656, Jul. 2002, doi: 10.1021/la025714x.

[120] P. Steins, A. Poulesquen, O. Diat, and F. Frizon, "Structural Evolution during Geopolymerization from an Early Age to Consolidated Material," *Langmuir*, vol. 28, no. 22, pp. 8502–8510, Jun. 2012, doi: 10.1021/la300868v.

[121] P. S. Singh, M. Trigg, I. Burgar, and T. Bastow, "Geopolymer formation processes at room temperature studied by 29Si and 27Al MAS-NMR," *Materials Science and Engineering: A*, vol. 396, no. 1, pp. 392–402, Apr. 2005, doi: 10.1016/j.msea.2005.02.002.

[122] M. Lahoti, K. K. Wong, E.-H. Yang, and K. H. Tan, "Effects of Si/Al molar ratio on strength endurance and volume stability of metakaolin geopolymers subject to elevated temperature," *Ceramics International*, vol. 44, no. 5, pp. 5726–5734, Apr. 2018, doi: 10.1016/j.ceramint.2017.12.226.

[123] J. Li *et al.*, "Curing process and pore structure of metakaolin-based geopolymers: Liquid-state 1H NMR investigation," *Cement and Concrete Research*, vol. 143, p. 106394, May 2021, doi: 10.1016/j.cemconres.2021.106394.

[124] P. Duxson, J. L. Provis, G. C. Lukey, S. W. Mallicoat, W. M. Kriven, and J. S. J. van Deventer, "Understanding the relationship between geopolymer composition, microstructure and mechanical properties," *Colloids and Surfaces A: Physicochemical and Engineering Aspects*, vol. 269, no. 1, pp. 47–58, Nov. 2005, doi: 10.1016/j.colsurfa.2005.06.060.

[125] Q. Wan *et al.*, "Geopolymerization reaction, microstructure and simulation of metakaolin-based geopolymers at extended Si/Al ratios," *Cement and Concrete Composites*, vol. 79, pp. 45–52, May 2017, doi: 10.1016/j.cemconcomp.2017.01.014.

[126] J. A. Ripmeester and C. I. Ratcliffe, "129Xe NMR spectroscopy in microporous solids: the effect of bulk properties," *Analytica Chimica Acta*, vol. 283, no. 3, pp. 1103–1112, Dec. 1993, doi: 10.1016/0003-2670(93)80268-P.

[127] K. E. Washburn and P. T. Callaghan, "Tracking Pore to Pore Exchange Using Relaxation Exchange Spectroscopy," *Physical Review Letters*, p. 4, 2006.

[128] J. Van Aelst *et al.*, "Hierarchization of USY Zeolite by NH4OH. A Postsynthetic Process Investigated by NMR and XRD," *J. Phys. Chem. C*, vol. 118, no. 39, pp. 22573–22582, Oct. 2014, doi: 10.1021/jp5058594.

Original publications

This thesis is based on the following publications, which are referred throughout the text by their Roman numerals:

I   Li, J., Mailhiot, S., Sreenivasan, H., Kantola, A. M., Illikainen, M., Adesanya, E., Kriskova, L., Telkki, V.-V., & Kinnunen, P. (2021). Curing process and pore structure of metakaolin-based geopolymers: Liquid-state ^1H NMR investigation. *Cement and Concrete Research*, 143, 106394. https://doi.org/10.1016/j.cemconres.2021.106394

II Li, J., Mailhiot, S., Sreenivasan, H., Kantola, A. M., Telkki, V.-V., & Kinnunen, P. (2022). 129Xe NMR analysis reveals efficient gas transport between inborn micro-, meso- and macropores in geopolymers. Cement and Concrete Research, 155, 106779. https://doi.org/10.1016/j.cemconres.2022.106779

III Li, J., Mailhiot, S., Kantola, A. M., Niu, H., Sreenivasan, H., Telkki, V.-V., & Kinnunen, P. (2022). Longitudinal single-sided NMR study: silica-to-alumina ratio changes the reaction mechanism of geopolymer [Manuscript submitted for publication].

IV Li, J., Mailhiot, S., Alzeer, M. I. M., Luukkonen, T., Niu, H., Kantola, A. M., Telkki, V.-V., & Kinnunen P. (2022). The effect of NH4OH treatment to the pore structure of geopolymer detected by 129Xe and 1H NMR method [Manuscript in preparation].

Original publications are not included in the electronic version of the dissertation.

---

819. Tervo, Nuutti (2022) Concepts for radiated nonlinear distortion and spatial linearization in millimeter-wave phased arrays

820. Nissilä, Tuukka (2022) Ice-templated cellulose nanofiber structures as reinforcement material in composites

821. Yu, Zitong (2022) Physiological signals measurement and spoofing detection from face video

822. Chen, Haoyu (2022) Human gesture and micro-gesture analysis : datasets, methods, and applications

823. Khan, Iqra Sadaf (2022) Exploring Industry 4.0 and its impact on sustainability and collaborative innovation

824. Peng, Wei (2022) Automatic neural network learning for human behavior understanding

825. Zhang, Ruichi (2022) Vanadium removal and recovery from liquid waste streams

826. Väätäjä, Maria (2022) Prospects of the room temperature fabrication method for electroceramics : feasibility for printing techniques and integration with temperature-sensitive materials

827. Li, Yante (2022) Machine learning for perceiving facial micro-expression

828. Behzad, Muzammil (2022) Deep learning methods for analyzing vision-based emotion recognition from 3D/4D facial point clouds

829. Leppänen, Tero (2022) From industrial side streams to the circular economy business : value chain, business ecosystem and productisation approach

830. Tuomela, Anne (2022) Enhancing the safety and surveillance of tailings storage facilities in cold climates

831. Kumar, Dileep (2022) Latency and reliability aware radio resource allocation for multi-antenna systems

832. Niu, He (2022) Valorization of mining wastes in alkali-activated materials

833. Jayasinghe, Laddu Praneeth Roshan (2022) Coordinated multiantenna interference mitigation techniques for flexible TDD systems

834. Zhu, Ruixue (2022) Interaction peculiarities of red blood cells and hemorheological alterations induced by laser radiation

835. Kuosmanen, Elina (2022) Technological support for Parkinson's disease patients' self-care